Department of Physics and Astronomy

University of Heidelberg

Master's thesis in Physics

submitted by

Malte Seán Andreas Buschmann

born in Freie und Hansestadt Hamburg

2014

Top Mass Effects in the Higgs–Gluon Coupling: Boosted vs. Off–Shell Production

This master's thesis has been carried out by Malte Buschmann
at the
Institute for Theoretical Physics, Heidelberg
and at the
Institute for Particle Physics Phenomenology, Durham (UK)
under the supervision of
Herrn Prof. Tilman Plehn

Top Mass Effects in the Higgs–Gluon Coupling:
Boosted vs. Off–Shell Production

Gluon fusion is one of the major Higgs production mechanism at the LHC. It is dominantly induced by top quark loops and can develop a logarithmic dependence on the top mass. Top mass effects occur for a boosted Higgs in association with jets in transverse momentum distributions, as well as for an off–shell Higgs in its reconstructed invariant mass. First, we study the logarithmic structure in the boosted Higgs regime for the two–jet case and compare it to previous one–jet results. We show that in the $H \to WW$ and $H \to \tau\tau$ decay channel, a corresponding analysis benefits immensely from the second jet in relevant rate and background rejection. Additionally, we present preliminary results of an inclusive simulation with all jet bins and state–of–the–art next–to–leading order corrections. Next, we study the top mass effects in the off–shell regime for a $H \to ZZ \to 4\ell$ decay and estimate the sensitivity of searches for contributions beyond the Standard Model.

Top–Massen–Effekte in der Higgs–Gluon Kopplung:
Boosted vs. Off–Shell Produktion

Gluon–Fusion ist eines der Hauptmechanismen zur Higgsproduktion am LHC. Sie ist hauptsächlich durch Top–Quark–Loops induziert, was zu logarithmischen Abhängigkeiten von der Top–Masse führen kann. Top–Massen–Effekte treten sowohl bei einem “boosted” Higgs in Zusammenhang mit Jets in transversalen Impulsverteilungen auf, als auch bei einem “off–shell” Higgs in dessen rekonstruierter invarianter Masse. Zunächst betrachten wir die logarithmische Struktur im “boosted” Regime für Prozesse mit zwei Jets und vergleichen diese mit alten Resultaten mit nur einem Jet. Wir zeigen, dass im Falle der Zerfallskanäle $H \to WW$ und $H \to \tau\tau$ eine zugehörige Analyse stark vom zweiten Jet sowohl in Rate als auch Hintergrundunterdrückung profitiert. Zusätzlich präsentieren wir vorläufige Resultate einer Simulation mit allen Jet–Bins und aktuellen “next–to–leading order” Korrekturen. Anschließend betrachten wir Top–Massen–Efffekte im “off–shell” Regime für einen $H \to ZZ \to 4\ell$ Zerfall und schätzen die Sensitivität von Suchen nach Beiträgen jenseits des Standard Modells.

Contents

1 Introduction

The discovery of the Higgs boson on the 4th of July 2012 at the Large Hadron Collider (LHC) [1, 2] was one of the biggest achievements of particle physics in recent decades. The Higgs boson was proposed in the 1960s in order to give particles of the Standard Model mass without violating fundamental gauge symmetries [3–7]. Yet, it took almost 50 years to produce and measure it. While the discovery was certainly a milestone, it just marks the beginning of many upcoming measurements. We already know that the Higgs is relatively light with a mass of around 125 GeV, has a narrow decay width [8] and favours the spin–0^+ hypothesis [9]. But many other properties are still unknown and some of them open doorways to completely new knowledge.

A precise measurement of the top Yukawa coupling is of particular interest, as it has a huge influence on our understanding of the Brout–Englert–Higgs mechanism. This coupling is crucial when extrapolating to more fundamental energy scales, which leaves space for new physics [10–13]. But a proper direct measurement of the top Yukawa coupling in tree–level processes is challenging, since it requires a good reconstruction of heavy states in rare associated Higgs and top production [14–26]. Even in the upcoming LHC runs this will be difficult. Additionally, from the theoretical point of view, our understanding of the top Yukawa coupling is strongly model–dependent [27–42].

However, already the Higgs discovery relied on processes, which are not realized at tree–level: Higgs production via gluon fusion and the $H \to \gamma\gamma$ decay channel. These kind of interactions are induced by loops of heavy particles, dominantly the W and top, thus inherit information about the Yukawa coupling. Especially gluon fusion, where the top is the only dominant loop particle in the Standard Model, has unique properties [43–46]. The loop in gluon fusion does not decouple for heavy particles, thus one can constrain new contributions to the Standard Model in form of heavy states. This effective coupling of gluons to the Higgs can be used to indirectly measure the top Yukawa coupling or to hunt new physics [47–50].

In this thesis we have a careful look at the Higgs–gluon coupling. We try to resolve the loop structure in order to get a deeper understanding of these higher dimensional interactions and how they can be used to constrain new physics. The basic idea is to derive effects, which are unique to a top mediated Higgs–gluon coupling. By comparing this to an effective dimension–6 coupling in the low energy Higgs effective field theory (HEFT) approximation [43–46], it is possible to calculate constraints on for instance new heavy loop particles. In this effective coupling the top loop is integrated out, such that no top related effects can occur. The same

is expected for contributions of new physics, thus they can be probed in a model independent way via the HEFT approximation [47, 48].

This approach is not new, as it was suggested already for a Higgs, which gets produced in association with a jet [47–49, 51, 52]. In this Hj process, a top mass dependent logarithmic structure occurs, which gets numerically significant in the boosted Higgs regime. However, we want to expand this to the more complex Hjj process, where completely new loop structures are possible. We compare both processes to see, which hard process is most sensitive when used in an actual analysis. This is the basis for more sophisticated and inclusive analyses, which take several jet bins into account. Based on our result, that the Hjj process is indeed more important than the Hj process, we show preliminar results with up to two jets to next–to–leading order (NLO) including the top mass effects.

Additionally to the boosted Higgs regime, we use the same ansatz for a Higgs, which gets produced off-shell. The $pp(\to H) \to ZZ \to 4\ell$ channel was recently explored by ATLAS and CMS using the off-shell regime mainly for Higgs width measurements [53–58]. But it is known that also in this regime top mass dependent logarithms occur [59, 60]. We want to investigate their numerical impact and how they compare with the boosted Higgs regime.

In Chapter 2 we give a brief overview about the concepts behind the Standard Model as well as Monte–Carlo simulations and confidence levels. Top mass effects in the boosted Higgs regime are described in Chapter 3. We first present our framework and derive the logarithmic structure. Their numerical impact on differential distributions of the Hjj and Hj process are compared and basic signal–background analyses are carried out for the decay channels $H \to WW$ and $H \to \tau\tau$. Both processes are compared by computing exclusion limits. Afterwards we present preliminary results of NLO simulations, where different jet multiplicities are merged. Next, we focus on the off-shell Higgs regime in Chapter 4 using the $H \to ZZ \to 4\ell$ channel. We present the framework and show the occurring top mass effects. With a basic statistical analysis we compute confidence levels. Finally we comment on the model–dependence of the off-shell Higgs width measurements.

2 Theoretical Concept

2.1 The Standard Model

The Standard Model of particle physics is the current theory to describe elementary particles and their interactions. It works within the framework of quantum field theory (QFT) and its predictions are tested in various different experiments to very high precision. The particle content comprise fermions, *i.e.* quarks and leptons, gauge bosons and the Higgs boson. The following part tries to give an understanding of the basic concepts on which the Standard Model is based. Of course, many important topics are not covered as we will focus mainly on those who are crucial for the actual thesis.

The Standard Model contains a fermionic Lagrangian, which in a free field theory can be written as

$$\mathcal{L} = \bar{\psi}\left(i\partial\!\!\!/ - m_\psi\right)\psi. \tag{2.1}$$

Such a non–interacting theory is obviously not very interesting but the theory comes alive when we require it to respect internal gauge symmetries. This essentially means the Lagrangian has to be invariant under symmetry transformation. As an illustrative example we can introduce a special unitary transformation $SU(N)$, where we transform the fermion fields like

$$\psi \to U(\alpha)\psi \quad \text{and} \quad \bar{\psi} = \bar{\psi}U^\dagger(\alpha) \qquad \text{with} \qquad U(\alpha) = e^{ig\alpha_a T^a}. \tag{2.2}$$

$\alpha_a T^a$ is a linear combination of the $N^2 - 1$ generators of the $su(N)$ algebra, obeying the commutator relation

$$\left[T^a, T^b\right] = if^{abc}T_c \tag{2.3}$$

with structure function f^{abc}. While such a global symmetry transformation trivially leaves the Lagrangian in Eq. (2.1) invariant, this is not true for a local transformation, *i.e.* with space–time dependent parameters $\alpha_a(x)$. In this case we get extra terms from the partial derivate in the Dirac operator $i\partial\!\!\!/ - m_\psi$, which we can absorb by replacing the partial derivate

by a covariant derivative

$$\partial^\mu \rightarrow D^\mu = \partial^\mu - igA_a^\mu T^a. \tag{2.4}$$

Here we introduce the gauge fields A_a^μ. They not only ensure that the Lagrangian stays invariant, but they also induce interactions with the fermion fields. The gauge fields are therefore also known as force carriers.

Since we have introduced new fields we have to think about which other terms we can write down in our Lagrangian including these fields. It turns out that the only allowed term with correct mass dimension and transformation property is

$$\mathcal{L}_{\text{gauge}} = -\frac{1}{2}\text{Tr}\left(F_{\mu\nu}F^{\mu\nu}\right) \tag{2.5}$$

with the field strength tensor

$$F_{\mu\nu}^a = \partial_\mu A_\nu^a - \partial_\nu A_\mu^a. \tag{2.6}$$

$\mathcal{L}_{\text{gauge}}$ is known as the kinematic term for gauge fields. By constructing the dual field strength tensor $\tilde{F}_{\mu\nu} = \epsilon^{\mu\nu\rho\sigma}F_{\rho\sigma}$ it would be possible to add a second term being consistent to our requirements. However, this term proportional to $\tilde{F}_{\mu\nu}F^{\mu\nu}$ is CP-odd which is not observed in experiment. It is therefore often not considered as part of the Standard Model Lagrangian. In this way gauge theory is able to describe the dynamics between particles. The procedure to construct the Standard Model Lagrangian is to choose the right gauge group and ultimately write down all allowed terms.

The full gauge group of the current Standard Model is a $SU(3)_c \times SU(2)_L \times U(1)_Y$ group, describing all known forces except gravity. The $SU(3)_c$ symmetry acts only on quarks and represents the strong force with gluons as the gauge particles. This part of the Standard Model is explained in Sec. 2.1.1 in terms of quantum chromodynamics (QCD). The combined $SU(2)_L \times U(1)_Y$ group is the electroweak symmetry, gets spontaneously broken and leads to the gauge bosons $W^\pm$, Z and γ. The breaking is induced by the Higgs field and the underlying mechanism is explained in Sec. 2.1.2.

2.1.1 QCD

QCD is based on a non–abelian $SU(3)_c$ symmetry, where the gauge parameter c represents the colour charge. The Lagrangian can be written as

$$\mathcal{L}_{\text{QCD}} = \mathcal{L}_{\text{quarks}} + \mathcal{L}_{\text{gauge}} + \mathcal{L}_{\text{gauge–fixing}} + \mathcal{L}_{\text{ghost}} \tag{2.7}$$

with

$$\mathcal{L}_{\text{quarks}} = \sum_{\text{flavour}} \bar{q}_a \left(i \not{D}_{ab} - m_{q_a} \delta_{ab} \right) q_b \qquad \mathcal{L}_{\text{gauge}} = \frac{1}{4} G^A_{\mu\nu} G^{\mu\nu}_A \tag{2.8}$$

$$\mathcal{L}_{\text{gauge–fixing}} = -\frac{1}{2\lambda} \left(\partial^\mu G^A_\mu \right)^2 \qquad \mathcal{L}_{\text{ghost}} = \left(\partial_\mu \eta^A \right)^\dagger \left(D^\mu_{AB} \eta^B \right). \tag{2.9}$$

$\mathcal{L}_{\text{quarks}}$ is the gauge theory coupled to fermionic matter, where q_a represents the quark fields. The covariant derivative is defined analogue to Eq. (2.4) in the fundamental representation as

$$D^\mu_{ab} = \partial^\mu \delta_{ab} - i g_s G^\mu_C t^C_{ab} \tag{2.10}$$

with the gluon field G^μ_C. The gluon field strength tensor used in the pure gauge part $\mathcal{L}_{\text{gauge}}$ is given in the adjoint representation by

$$G^A_{\mu\nu} = \partial_\mu G^A_\nu - \partial_\nu G^A_\mu - g_s f^{ABC} G^B_\mu G^C_\nu \tag{2.11}$$

with the QCD coupling strength g_s. With the kinematic part of $\mathcal{L}_{\text{gauge}}$ the gluon propagator is not defined properly and therefore $\mathcal{L}_{\text{gauge–fixing}}$ has to be added to the Lagrangian. There, λ is an arbitrary parameter which is often chosen to be $\lambda = 1$ (Feynman gauge) or $\lambda \to 0$ (Landau gauge). The last contribution $\mathcal{L}_{\text{ghost}}$ introduces Fadeev–Popov ghosts η^A, which are necessary to cancel unphysical longitudinal degrees of freedom in a non–abelian theory. Those complex scalar fields appear only as virtual particles and do not correspond to any real particle in external states. By redefining the gauge–fixing term in principle no ghost term would be required. But this would lead to a more complex gluon propagator such that the preferable choice is usually the introduction of ghosts.

In Eq. (2.10) the strong coupling constant $\alpha_s = g_s^2/4\pi$ is introduced. During the calculation of observables as a perturbation series in α_s ultraviolet divergences will appear. Renormalization group theory tells us that when trying to remove those divergences we have to introduce a unphysical mass scale μ_R, on which the coupling constant will depend. Since our renormalization parameter μ_R is arbitrary this parameter should not appear in the end result. Using the β–function approach the μ_R^2 dependence of α_s is translated into a dependence of the physical parameter Q^2 via

$$\alpha_s \left(Q^2 \right) = \frac{\alpha_s \left(\mu_R^2 \right)}{1 + \alpha_s \left(\mu_R^2 \right) \beta_0 \ln \left(Q^2 / \mu_R^2 \right)}. \tag{2.12}$$

The function β_0 depends solely on the number of quark flavours with mass lower than μ_R. Hence, the results is an energy scale dependent coupling α_s.

This so–called *running of the coupling* is important because it defines two different regimes. For large Q^2 the coupling strength will decrease, known as *asymptotic freedom*. Therefore it is possible to do a perturbation series in α_s for large momentum transfer Q. On the other

hand, for small Q^2, the coupling will increase and no perturbation theory is applicable. This regime is known as *confinement*.

Asymptotic freedom and confinement are playing a particularly important role in predicting observables in the environment of a hadron collider. At a collider both regimes are involved, but QCD has different powers of predictability for them. For high energies we can perform a perturbative expansion and therefore analytically calculate a process for different orders in α_s separately. At low energies however, the QCD effects are not as well understood as in the high energy regime. We rely on data and models of the non–perturbative behaviour to describe for example parton distribution functions (PDFs).

For a proper prediction at a collider both regimes have to be taken into account. The factorization theorem describes how the perturbative and the non–perturbative part can be separated. The downside is the introduction of another unphysical scale μ_F, which defines the threshold between hard and soft QCD. This factorization parameter μ_F is often chosen to be of order of the typical momentum scale of a chosen process.

2.1.2 Breaking the Electroweak Symmetry

After we have discussed QCD and its underlying $SU(3)_c$ symmetry, we now want to give a brief introduction in the electroweak $SU(2)_L \times U(1)_Y$ symmetry group and how it is spontaneously broken in the Standard Model.

The label Y of the $U(1)$ symmetry is the hypercharge, whereas the label L corresponds to the chiral nature of the $SU(2)$ symmetry. From experiment we know that only left–handed quarks interact with the weak gauge bosons of the $SU(2)$ symmetry. Left–handed chiral fields ψ_L are projected from the fermion fields using the projection operator P_L

$$\psi_L = P_L \psi = \frac{1}{2}\left(1 - \gamma_5\right)\psi, \tag{2.13}$$

where $\gamma_5 = i\gamma_0\gamma_1\gamma_2\gamma_3$. Using left–handed doublets $Q_L = \begin{pmatrix} u_L & d_L \end{pmatrix}^T$ and right–handed singlets u_R and d_R for up–type and down–type quarks, the kinematic part of the electroweak Lagrangian can be written as

$$\mathcal{L}_{\text{kin}} = i\bar{Q}_L \not{D}_L Q_L + i\bar{u}_R \not{D}_R u_R + i\bar{d}_R \not{D}_R d_R. \tag{2.14}$$

In a similar way the leptonic Lagrangian can be written down for the doublets $L_L = \begin{pmatrix} \nu_L & \ell_L \end{pmatrix}^T$ and singlets ℓ_R. Right–handed neutrinos are not observed. The covariant derivatives in Eq. (2.14) are in terms of the $SU(2)_L \times U(1)_Y$ basis

$$D_{L\mu} = \partial_\mu - ig' Y B_\mu - igW_{\mu a}\tau^a \tag{2.15}$$

$$D_{R\mu} = \partial_\mu - ig' Y B_\mu, \tag{2.16}$$

representing the fact that the right–handed particles are a singlet under the $SU(2)_L$ group. $W_{\mu a}$ and B_μ are the gauge fields corresponding to the $SU(2)_L$ and $U(1)_Y$ respectively, with the rescaled Pauli matrices τ^a as the generators of the $SU(2)$ symmetry group. Those four gauge fields are not yet the physical fields observed. They have to be rotated in their mass eigenstates using the Weinberg angle Θ_w, creating the photon field A_μ, Z field Z_μ and W fields $W^\pm_\mu$,

$$\begin{pmatrix} A_\mu \\ Z_\mu \end{pmatrix} = \begin{pmatrix} \cos\Theta_w & \sin\Theta_w \\ -\sin\Theta_w & \cos\Theta_w \end{pmatrix} \begin{pmatrix} B_\mu \\ W^3_\mu \end{pmatrix}, \qquad W^\pm_\mu = \frac{1}{\sqrt{2}} \left(W^1_\mu \mp i W^2_\mu \right). \tag{2.17}$$

Since right–handed and left–handed quark fields transform differently under the $SU(2)_L$ group, it is not possible to write down a gauge invariant mass term proportional to $\bar{Q}_L m_Q Q_R$. The same is also true for the gauge fields, but we do know that those particles have mass. To solve this problem the complex scalar field ϕ is introduced with four additional degrees of freedom. We give this field a kinematic term and a potential,

$$\mathcal{L}_\phi = \left(D^\mu \phi\right)^\dagger \left(D_\mu \phi\right) - \mu^2 \left|\phi\right|^2 - \lambda \left|\phi\right|^4. \tag{2.18}$$

This potential is, due to its characteristic shape, also known as Mexican–Hat potential. The prefactors $\lambda > 0$ and $\mu^2 < 0$ are of mass dimension zero and two respectively. The ϕ doublet itself can be written in the linear representation as

$$\phi = \frac{1}{\sqrt{2}} \begin{pmatrix} -w_2 - i w_1 \\ v + H + i w_3 \end{pmatrix}. \tag{2.19}$$

The mass scale v has a particularly important role because the vacuum does not vanish when minimizing the potential of Eq. (2.18) for $v \neq 0$. v is therefore known as the vacuum expectation value (vev) and found to be 246 GeV. This non–vanishing vev, however, breaks the local $SU(2)_L \times U(1)_Y$ gauge symmetry spontaneously down to the smaller $U(1)_{\text{em}}$ group of electromagnetism. The fields w_i in Eq. (2.19) are a set of scalar Nambu–Goldstone modes and they correspond to the three broken generators of the initial $SU(2)_L \times U(1)_Y$ group. We broke a local gauge symmetry which means those Goldstone modes are 'eaten' by the gauge bosons $W^\pm$ and Z and that they will represent their longitudinal polarization component. Because there are more Goldstone modes than degrees of freedom for the gauge bosons an additional scalar degree of freedom appears, the Higgs boson H.

By constructing the Yukawa interaction Lagrangian for fermions

$$\mathcal{L}_{\text{Yukawa}} = -y_\psi \left(\bar{\psi}_L \phi \psi_R + \bar{\psi}_R \phi \psi_L \right) \tag{2.20}$$

we not only write down an interaction term for the Higgs field with fermions, but also well defined mass terms for the fermions proportional to $y_\psi v$. By identifying the mass term, we

find that $y_\psi v = \sqrt{2} m_\psi$. Since the Yukawa coupling y_ψ also defines the coupling strength of the Higgs to fermions we see that the Higgs–fermion coupling is proportional to the fermion mass itself. The same feature is true for the coupling to gauge bosons, which is part of the kinematic term in Eq. (2.18). This coupling behaviour is phenomenologically relevant, as it makes the top particle and the heavy gauge bosons $W^\pm$ and Z important for Higgs analyses at tree level. But it is also delusive, as it turns out that even massless particles play an essential role numerically at loop level. One of such an interaction, which will be important throughout the thesis, is described in the next section.

2.1.3 Higgs–Gluon Coupling

Gluons are massless and therefore a Higgs–gluon coupling is not part of the renormalizable dimension–4 Lagrangian at tree level. At loop level though, this coupling can be induced by a closed top quark loop. In principle other fermions are running in the loop too, but their contributions are small due to the large top quark Yukawa coupling. This dimension–6 operator includes a coupling of the Higgs to two gluons and – because of the non–abelian nature of the $SU(3)_c$ group – even to three or four gluons. In terms of an effective Lagrangian the Higgs–gluon coupling can be expressed as

$$\mathcal{L}_{ggH} \supset g_{ggH} \frac{H}{v} G_{\mu\nu} G^{\mu\nu}, \tag{2.21}$$

with

$$\frac{g_{ggH}}{v} = \frac{\alpha_s}{8\pi} \frac{1}{v} \tau \left[1 + (1-\tau) f(\tau)\right], \qquad \tau = 4\frac{m_t^2}{m_H^2} > 1 \tag{2.22}$$

and the three–point function describing the top–loop

$$f(\tau) \overset{\text{on–shell}}{=} -\frac{m_H^2}{2} C(0, 0, m_H^2; m_t^2, m_t^2, m_t^2) = \arcsin^2 \sqrt{\frac{1}{\tau}}. \tag{2.23}$$

The last equation assumes that all external particles are on its mass shell. A derivation of this coupling can be found for example in [46]. The used correlation integral for a top loop between two gluons and one Higgs can be written in a general way as

$$\begin{aligned} &C(k_{g_1}^2, k_{g_2}^2, k_H^2; m_t^2, m_t^2, m_t^2) \\ &\quad \equiv \int \frac{d^4 q}{(2\pi)^4} \frac{1}{[q^2 - m_t^2 - i\epsilon] \left[(q + k_{g_1})^2 - m_t^2 - i\epsilon\right] \left[(q + k_{g_1} + k_{g_2})^2 - m_t^2 - i\epsilon\right]}. \end{aligned} \tag{2.24}$$

The parameter g_{ggH} is dimensionful in order to make the dimension–5 operator of Eq. (2.21) part of the dimension–4 Lagrangian. Note that g_{ggH} is not proportional to $1/m_t$ but $1/v$, which is effectively due to the top Yukawa coupling occurring in the top loop. Generally

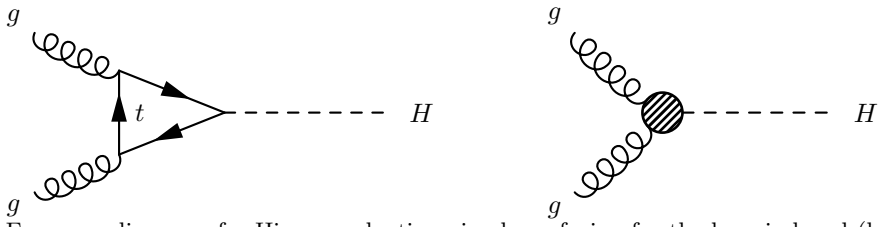

Figure 2.1: Feynman diagrams for Higgs production via gluon–fusion for the loop induced (left) and effective coupling (right).

speaking this means the Higgs–gluon coupling does not decouple for heavy quarks because it is not suppressed by a large energy scale. Hence, even heavier particles than the top can effectively contribute to the coupling without any additional suppression due to its large mass.

The above coupling depends on the top and Higgs mass and can be simplified in the heavy–top limit, $\tau \to \infty$, since $m_H < 2m_t$. Using the Taylor expansion

$$\arcsin^2\sqrt{\frac{1}{\tau}} \xrightarrow{\tau\to\infty} \frac{1}{\tau} + \frac{1}{3\tau^2} + \mathcal{O}\left(\frac{1}{\tau^3}\right) \qquad \Rightarrow \qquad \frac{g_{ggH}}{v} = \frac{\alpha_s}{12\pi}\frac{1}{v} \tag{2.25}$$

we get a more handy expression for the Higgs–gluon coupling

$$\mathcal{L}_{ggH} \supset \frac{\alpha_s}{12\pi}\frac{H}{v} G_{\mu\nu}G^{\mu\nu}, \tag{2.26}$$

where the top quark is not propagating anymore. This low energy Higgs effective field theory (HEFT) approximation is, as expected from the non–decoupling property, finite [43–45]. The deviation between the exact calculation and the HEFT approximation in the inclusive $gg \to H$ production rate at the LHC is typically within $\mathcal{O}(10\%)$ [61–67]. While the effective coupling constant g_{ggH} inherits full top mass dependence the above dimension–6 operator does not. All momentum dependence arises here from the gluon field strengths $G_{\mu\nu}G^{\mu\nu}$.

Note that the above calculation is valid only if all external particles are on–shell and with a triangle top–loop, as presented in the left panel of Fig. 2.1. Once one of the particles is off-shell the function $f(\tau)$ of Eq. (2.23) gets more complex and the three–point function of Eq. (2.24) develops a non–trivial dependence on the top mass [59, 60]. The HEFT approximation then breaks down. The same happens when we consider QCD effects and add an extra jet to the process. In this case we need to include a four–point correlation function to Higgs production [47, 48]. Also this leads to a break–down of the low–energy approximation to the dimension–6 operator.

In proton–proton collision at the LHC we have four major production processes of the Higgs; gluon fusion, weak boson fusion (VBF), Higgs strahlung and associated Higgs production. Despite the fact that the Higgs–gluon coupling is realized only at loop level, it turns out that gluon–fusion is numerically dominant at the LHC [68]. While this is partially due to

the large top Yukawa coupling and the large gluon probability in the PDFs of the proton at typical LHC energies, it makes this process an important study object. Especially the non–decoupling property links this coupling to searches beyond the Standard Model. But already for the Higgs discovery the pure dimension–6 interactions of the Higgs with gluons and photons had a large impact [1, 2].

2.2 Monte–Carlo Simulations

Monte–Carlo simulations are essential in particle physics, as they are the link between theory and experiment. The term *Monte–Carlo* refers to the technique of using random numbers and probability statistics. The simulations are based on theoretical models and have the ambition to reproduce experimental rates as well as shapes of differential distributions. Hence, they are used to probe theories by comparing Monte–Carlo simulations with experimental data.

The structure of such a Monte–Carlo simulation of pp collisions is mainly dictated by properties of QCD. As we have seen in Sec. 2.1.1 we get two different regimes when dealing with strong interactions, asymptotic freedom and confinement. One of them can be calculated perturbatively in orders of the strong coupling constant α_s, whereas the other one can not be calculated exactly. Therefore, a simple simulation starts with a so–called *hard process*, where a chosen matrix–element squared is calculated for a fixed order in α_s, according to the asymptotic freedom. Hence, the involved strong interactions show large momentum transfers, such that partons in the final state are hard, *i.e.* with high momentum.

Other kind of QCD radiation, including soft parton splitting and collinear gluon emission, is attached to the matrix element afterwards. An approximation scheme is used in this regime, kown as *parton shower*. The perturbative regime is convoluted with the non–perturbative PDFs, following the factorization theorem [69]. The factorization scale μ_F is used to separate between the energy scale used in the perturbative and non–perturbative regime.

After the hard process got showered hadronization takes place. All particles, which are not already stable, are then subsequently clustered to hadrons, forming a *jet*. This is done until the complete event consists of stable particles or particles with a lifetime longer than around 10 ps. This is long enough for them to reach the detector. The event can then be analysed and expressed in experimentally measurable observables.

Momenta of jets are one of the common observables in a LHC environment, but simulating them properly with the above scheme is difficult. Hard and soft jets are generated at different stages, either as part of the hard process or for instance the parton shower, separated by an ambiguous scale. Therefore, already the hard process has to be picked with much care in order to get meaningful results, since it defines the number of properly simulated hard jets. Hence, a calculation for a fixed order in α_s is often not desirable and often processes with

different numbers of final state multiplicities are merged. Great care has to be taken here in order to avoid double counting of jets when attaching a parton shower. Normally another scale, the merging scale μ_Q, is introduced.

Additionally, further corrections can be made by performing next–to–leading order (NLO) corrections. Leading order (LO) in this thesis will be always referring to LO in α_s of a chosen hard process, even though NLO corrections concerning the electroweak coupling constant can also be done. Those QCD NLO calculations add one additional order of α_s to the original born diagram. This includes diagrams with virtual loop corrections but also diagrams with additional radiation of a hard parton. It is a great task to match and merge jets from different origins in this case, however, the simulation results are then even closer to what we observe in experiment. Those corrections do normally change the total rate, but can also lead to shape differences of differential cross sections.

2.3 Confidence Levels

Statistics is a mathematical tool found everywhere in physics and is an essential part of particle physics. Since there is nothing like ultimate truth in experiment we rely on probabilities when it comes to discoveries or to the exclusion of models. In this thesis we want to constraint the contribution of new physics to the Standard Model and therefore we need to know with which confidence a model can be excluded. In the following paragraph we want to address the concept behind exclusion limits and confidence level plots.

We start with the so–called test hypothesis H_{BSM} as the Standard Model assuming new physics and the null hypothesis H_{SM} as the Standard Model only. We then can define the likelihood ratio

$$Q = \frac{P(\mathrm{data}|H_{\mathrm{BSM}})}{P(\mathrm{data}|H_{\mathrm{SM}})}, \tag{2.27}$$

where $P(\mathrm{data}|H_x)$ is the probability that a given data set is described by the hypothesis H_x. This probability is normally determined with a fit to the data and is maximized over the variation of possible nuisance parameters. The maximization can be translated into a minimization of the log–likelihood test statistic

$$\Delta\chi^2 = -2\ln Q = \chi^2(\mathrm{data}|H_{\mathrm{BSM}}) - \chi^2(\mathrm{data}|H_{\mathrm{SM}}), \tag{2.28}$$

where the nuisance parameters are varied separately for both hypotheses. With the confidence level for excluding the test hypothesis given some data and a null hypothesis,

$$CL_{H_{\mathrm{BSM}}} = P_{H_{\mathrm{BSM}}}(Q \leq Q_{\mathrm{obs}}) = P_{H_{\mathrm{BSM}}}(\Delta\chi^2 \geq \Delta\chi^2_{\mathrm{obs}}), \tag{2.29}$$

we can finally define the quantity of interest,

$$CL_s = \frac{CL_{H_{\mathrm{BSM}}}}{CL_{H_{\mathrm{SM}}}}. \tag{2.30}$$

Here, $P_x(\Delta\chi^2 \geq \Delta\chi^2_{\mathrm{obs}})$ corresponds to the probability that $\Delta\chi^2$ is greater than $\Delta\chi^2_{\mathrm{obs}}$ obtained from data for the hypothesis H_x. This probability is often determined via pseudo-experiments, which are analysed like the data. In our case, without having any real data, the null hypothesis itself represents the ensemble, from which those pseudoexperiments are drawn. The usual definition is that the hypothesis H_{BSM} is called excluded once the CL_s value drops below 0.05, known as the 95% confidence level limit.

3 Boosted Higgs Production

3.1 Framework

As we have seen in Sec. 2.1.3 the Higgs–gluon coupling does not decouple for heavy particles. This property can be used to hunt for instance additional hypothetical heavy particles and eventually rule out their existence. One question might be if, beside light quarks, the top is really the only heavy loop particle contributing to the Higgs–gluon coupling we have measured at the LHC. We therefore want to study the nature of the this coupling in a model–independent way. We want to see for instance whether the top Yukawa coupling is indeed responsible of for the observed Higgs–gluon coupling. The description of the coupling, including the full loop integral, of course depends on a given model. The HEFT approximation of Eq. (2.26) holds, however, for any loop contribution under the assumption that new physics can be integrated out [47, 48].

We therefore assume a new contribution, represented by the HEFT approximation, to the Higgs–gluon coupling,

$$\mathcal{L}_{ggH} \supset \left[\kappa_t g_{ggH} + \kappa_g \frac{\alpha_s}{12\pi}\right] \frac{H}{v} G_{\mu\nu} G^{\mu\nu} - \kappa_t \frac{m_t}{v} H \left(\bar{t}_R t_L + \text{h.c.}\right), \tag{3.1}$$

where the parameter set $(\kappa_t, \kappa_g) = (1, 0)$ reproduces the pure Standard Model. By modifying κ_g and κ_t such that their sum stays constant, it is possible to shift the contribution of the top to a new unspecified source. Note that by modifying the top Yukawa coupling the total observed Higgs cross section at the LHC is left unchanged. One possible new physics model which can be described by the above parametrisation would be the Standard Model with an extended Higgs sector and an unobserved heavy top partner [27, 28, 49]. Unless otherwise mentioned we will refer in the following to the three reference points

$$(\kappa_t, \kappa_g)_{\text{SM}} = (1, 0), \qquad (\kappa_t, \kappa_g)_{\text{BSM}} = (0.8, 0.2) \qquad \text{and} \qquad (\kappa_t, \kappa_g)_{\text{HEFT}} = (0, 1). \tag{3.2}$$

The set $(\kappa_t, \kappa_g)_{\text{BSM}}$ represents a more realistic parameterization for a scenario beyond the Standard Model (BSM).

Expressing Eq. (3.1) in terms of matrix elements for Higgs production in gluon fusion leads to the two terms

$$\mathcal{M} = \kappa_t \mathcal{M}_t + \kappa_g \mathcal{M}_g, \tag{3.3}$$

where all prefactors except $\kappa_{t,g}$ are absorbed into the definition of $\mathcal{M}_t$ and $\mathcal{M}_g$. All other tree–level Higgs interactions are kept unchanged for simplicity. A shift in the loop–induced Higgs–photon coupling is not phenomenological relevant, because the loop does not only involve QCD but also electroweak couplings. Due to the additional W loop it is difficult to extract informations about the top Yukawa coupling.

Translating the above equation in differential cross sections by squaring the matrix elements we get for any kinematic distribution

$$\frac{d\sigma}{d\mathcal{O}} = \kappa_t^2 \frac{d\sigma_{tt}}{d\mathcal{O}} + 2\kappa_t\kappa_g \frac{d\sigma_{tg}}{d\mathcal{O}} + \kappa_g^2 \frac{d\sigma_{gg}}{d\mathcal{O}}, \tag{3.4}$$

where $\mathcal{O}$ represents an arbitrary observable operator. Since in general $\kappa_t \gg \kappa_g$ the last term proportional to κ_g^2 can be numerically neglected for a BSM model. Hence, only the interference between the top–induced coupling and the HEFT component is of importance when testing the hypothesis.

The key question is how to resolve the coupling and ultimately, if the parameters κ_t and κ_g differ from the Standard Model values. When only the Higgs is produced in gluon fusion we can already see from the coupling g_{ggH} that the process will depend only on the Higgs and top mass. There is for instance nothing the Higgs could recoil against. But if the Higgs is produced together with additional partons as part of the hard process the corresponding Feynman diagrams are more complex. The coupling will then develope a dependence on the kinematics of the external states [47, 48]. Since the kinematics will therefore differ between the exact loop calculation and the HEFT approximation, additional jets allow us to extract information about the Higgs–gluon coupling.

This is our main motivation why we will consider jets as part of the hard process calculation. Past studies showed that effects in the boosted Higgs regime, *i.e.* a Higgs with large transverse momentum, are expected for events based on a matrix–element which includes one jet [47–49, 51, 52]. We want to further exploit the impact of this effect, but mainly extend the study to Higgs production in gluon fusion in association with two jets. Because these effects are only present in the boosted regime, the proper description of a second hard jet might turn out to be important.

Event samples at parton level for both processes are generated for the SM, BSM and HEFT hypothesis according to Eq. (3.2). We used MCFM [70, 71] for the Hj process and VBFNLO [72–74] for Hjj at a center of mass energy of $\sqrt{s} = 13$ TeV for the generation of Monte Carlo events. Both generators provide results for the SM (finite top mass) and HEFT (pure dimension–6) scenario. In order to construct the BSM hypothesis, both implementations had to be expanded by the interference term. The dimension–6 modifications to MCFM were validated against the independent implementation in VBFNLO. The PDF set CTEQ6L1 [75] is used and the data is analyzed and plotted using the ROOT package [76].

These calculations are performed at LO, since no NLO corrections including the full top

mass dependence were available at that time. Nevertheless, further studies with NLO implementations are performed in Sec. 3.4 with developmental SHERPA+OPENLOOPS [77–83] samples. In order to account for the missing NLO corrections we rescaled the total LO cross section with a factor of $K_{Hj} = 1.4$ [70, 71] and $K_{Hjj} = 1.6$ [84–86], respectively. It is known that NLO corrections, including top mass dependencies, do change distributions only within $\mathcal{O}(10\%)$ in comparison to a LO implementation, even for a boosted Higgs [66].

3.2 Top Mass Effects

Total rates are unchanged, therefore we rely on shape difference in differential distributions. There are different ways how a top loop can effect distributions. A threshold enhancement due to the top mass, which we will describe in more detail in the off-shell chapter, in the invariant masses m_{Hj} and m_{Hjj} do exist. But we found that it is numerically small and does not allow us to make any statement about the origin of the Higgs–gluon coupling. More promising is the approach of top mass induced logarithms.

When the Higgs is produced in association with a hard jet the low energy field theory approximation is strictly speaking no longer valid. Diagrams, in which a gluon is radiated by one of the loop particles do not exist. Those more complex diagrams involve additional scalar integrals, leading to additional top mass dependent logarithmic terms. The same is true for diagrams where the gluons are off–shell. To understand the effects of the missing mass scale m_t we have to take a closer look at the analytic form of the 1–jet and 2–jet matrix element when top mass effects are taken into account.

3.2.1 Logarithmic Structure

For the Hj process, the cross section of the partonic subprocess $gg \to Hg$ can be written as

$$\sigma_{gg\to Hg} = \frac{\beta_H}{16\pi s}\frac{\alpha_s^3}{4\pi v^2}\frac{3}{2}\sum_{\lambda_i=\pm}\left|\mathcal{M}_{\lambda_1\lambda_2\lambda_3}\right|^2, \tag{3.5}$$

neglecting quarks in the loop other than the top [51]. β_H denotes the final state velocity and $\lambda_i = \pm$ are the helicities of the three involved gluons. Looking at the helicity configuration $\mathcal{M}_{+++}$ it is possible to show that it can be expressed as

$$\mathcal{M}_{+++} \propto \frac{m_t^2\kappa}{p_T}\left[A_0 + A_1\ln\left(\frac{p_T^2}{m_t^2}\right) + A_2\ln^2\left(\frac{p_T^2}{m_t^2}\right)\right] \tag{3.6}$$

in the high energy limit $p_T = p_{T,H} = p_{T,j} \gg m_H, m_t$. A derivation of this structure can be found in the Appendix. The parameter κ is related to the top Yukawa coupling $y_t = \kappa m_t/v$ and A_i are a combination of constants and top mass independent logarithms. For high p_T,

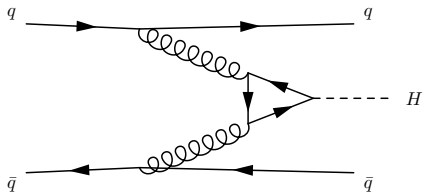

Figure 3.1: Feynman diagram for the $q\bar{q} \to Hq\bar{q}$ process with its VBF–like topology. The participating gluons can be highly virtual.

we therefore conclude that the leading term for this subprocess scales like

$$\sigma_{gg\to Hg} \propto m_t^4 \ln^4\left(\frac{p_T^2}{m_t^2}\right). \tag{3.7}$$

Such logarithmic dependence on the transverse momentum is present only in case of a top quark loop. If for instance additional particles are also inducing the Higgs–gluon coupling, *i.e.* $k_g \neq 0$, this logarithmic structure does not occur in this form. For the HEFT approximation the top mass scale is missing and thus the logarithms are completely absent. This means an additional jet can be used to probe the coupling in the boosted Higgs regime and potentially disentangle the coupling modifications κ_t and κ_g [49, 51, 52, 87].

For the Hjj process, the two jets result in several external mass scales, which makes the situation more complex. It is not yet clear which kind of invariant is responsible for a logarithmic top mass dependence. Picking the simplest subprocess, $q\bar{q} \to Hq\bar{q}$, in principle only the effective Higgs–gluon coupling can be probed. The two jets are in this VBF–like topology not attached to the loop itself, as it can be seen in Fig. 3.1. The major difference, however, is that the gluons from the incoming parton splitting can be highly virtual, changing the scaling behaviour of the corresponding scalar three point function. Expressed in terms of the virtualities $Q_{1,2} > 0$ of the two space–like or t–channel gluons we find

$$\sigma_{q\bar{q}\to Hq\bar{q}} \propto \frac{m_t^4}{\left(Q_1^2 - Q_2^2\right)^2}\left[\ln^2\left(\frac{Q_1^2}{m_t^2}\right) - \ln^2\left(\frac{Q_2^2}{m_t^2}\right)\right]^2 \overset{Q_1 \gg Q_2}{=} \frac{m_t^4}{Q_1^4}\ln^4\left(\frac{Q_1^2}{m_t^2}\right). \tag{3.8}$$

In the collinear limit, the virtuality dependence can be translated into a dependence of the transverse momentum [88]. In case of unbalanced jets recoiling against the Higgs, $Q_1 \gg Q_2$, the above logarithm reproduces the logarithm occurring in the 1-jet matrix element,

$$\sigma_{q\bar{q}\to Hq\bar{q}} \propto m_t^4 \ln^4\left(\frac{p_{T,j}^2}{m_t^2}\right) \sim m_t^4 \ln^4\left(\frac{p_{T,H}^2}{m_t^2}\right). \tag{3.9}$$

Here, a linear relation between Q_1 and p_T is assumed, following the calculations of [88].

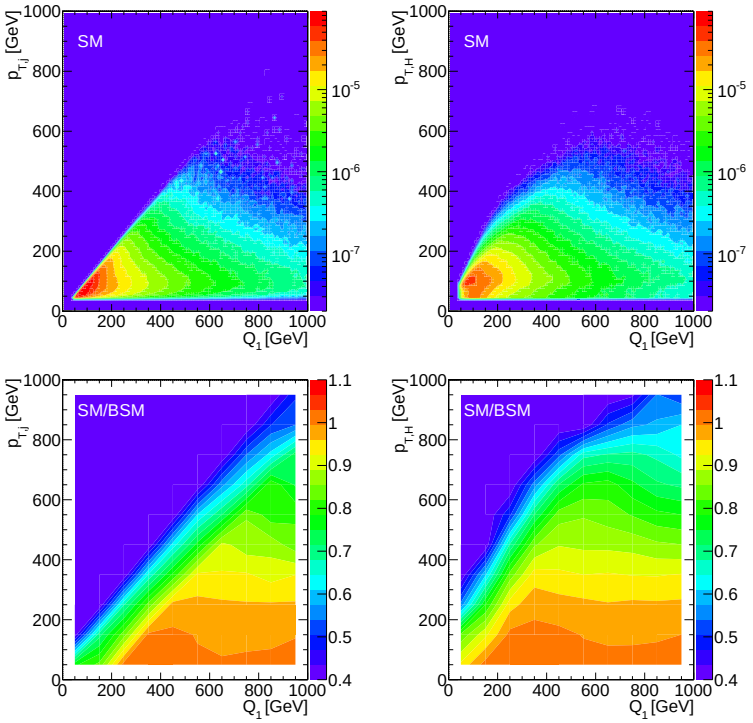

Figure 3.2: correlation plots for the $p_{T,j}$ vs Q_1 (left) and $P_{T,H}$ vs Q_1 (right) for Hjj production in the Standard Model, $\kappa_{t,g} = (1, 0)$. We also show the ratio SM/BSM (bottom row), where BSM is defined as $\kappa_{t,g} = (0.8, 0.2)$.

3.2.2 Parton Level Simulation

In the upper panel of Fig. 3.2 we present the correlation between the gluon virtuality and the transverse momentum of the leading jet or the Higgs at parton level. As expected from kinematic constraints we observe no events for $p_{T,j} > Q$ for the Hjj process. This clear boundary is washed out slightly for $p_{T,H}$, since the Higgs can get a boost from the the second gluon. The overall kinematic distribution agrees well with the considerations of [88]. The lower panel of Fig. 3.2 shows for both correlation plots the ratio SM/BSM, which we expect to differ from one due to the different logarithmic structure for both hypotheses. While the ratio starts around one for small transverse momentum it goes down for a boosted jet or Higgs, as expected from a purely p_T dependent logarithm. It is clearly visible that for the whole phase space the ratio is almost independent of the gluon virtuality. This shows that the logarithmic structure of the 2–jet matrix element and the 1–jet matrix element is indeed similar, as indicated by Eq. (3.7) and (3.9).

Keeping this observation in mind, the key questions is their numerical impact. To compare the Hj and Hjj matrix elements we have taken a look at various differential cross sections for the SM and BSM hypothesis. Fig. 3.3 shows that for both matrix elements the SM and BSM

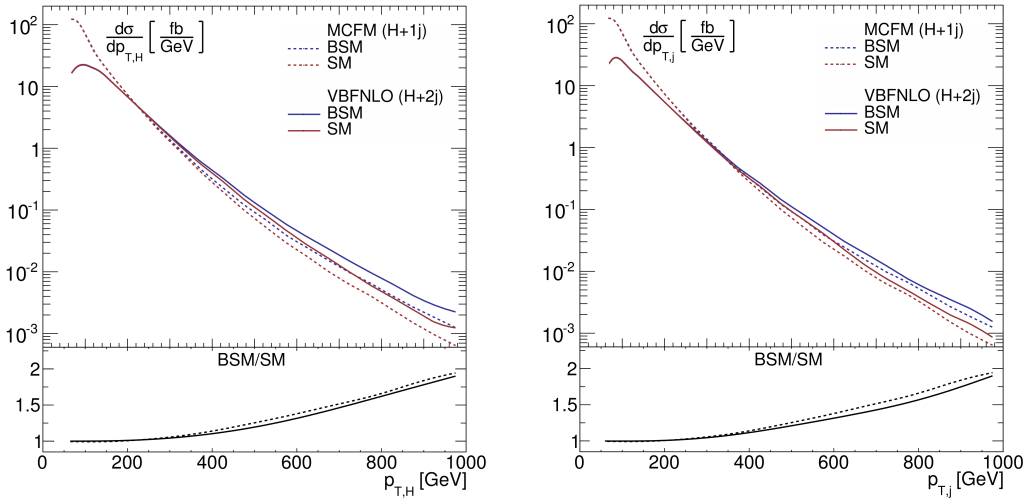

Figure 3.3: Parton–level $p_{T,H}$ (left) and p_{T,j_1} (right) distributions for Hj and Hjj production. The red curve corresponds to the Standard Model $\kappa_{t,g} = (1, 0)$, while the blue curves follow from the BSM hypothesis $\kappa_{t,g} = (0.8, 0.2)$. We assume $\sqrt{s} = 13$ TeV.

distributions are not showing any difference in the low energy regime. However, they start to split up for around 300 GeV, reaching a ratio of around two for a very boosted Higgs or leading jet of 1 TeV transverse momentum. As we have seen, both splittings are a result of a similar logarithmic structure and therefore the ratio BSM/SM does not show any significant difference between the Hj and Hjj process. Also, the ratio does not shows any difference between $p_{T,H}$ and $p_{T,j}$.

Nevertheless, despite the fact that the 1–jet matrix element has a higher total cross section than the 2–jet matrix element, it is an important observation that this extra contribution mainly leads to soft jets [89, 90]. Since we are sensitive only in the boosted regime the higher total Hj cross section therefore does not help resolving the Higgs–gluon coupling. In fact, in the phase space region of interest the Hjj process is more dominant, indicating that the 2–jet matrix element is indeed of importance.

Showing that the Hjj process is more relevant in the boosted regime than the Hj process, we might have to think about even more jets. Of course we can only speculate about this without simulating the 3–jet case. But we can extract some hints from the 2–jet matrix element already by looking at different initial states. For the qq and gq initial state we have one–loop triangle and box diagrams contributing and only for the pure gluon amplitudes pentagon loops are possible. See for example Fig. 3.4. This allows us to determine the relative contribution of those more complex pentagon loops arising due to the second jet.

We observe that for the qq initial state the top mass effects are the strongest whereas they are weaker for the gg initial state, as presented in Fig. 3.5. This indicates that the top mass effects are mainly occurring in the VBF–like topology with a triangle loop as described be-

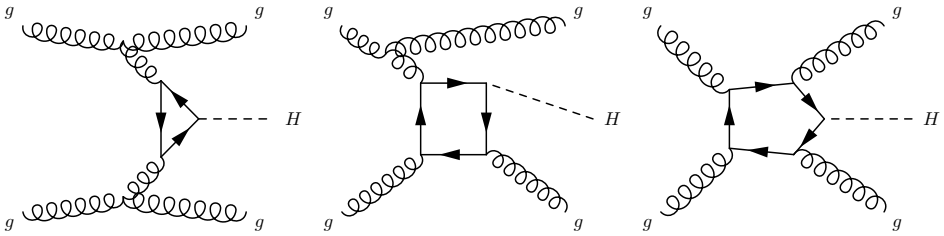

Figure 3.4: Sample diagrams for a triangle (left), box (middle) and pentagon (right) loop. A pentagon loop is only in case of $gg \to Hgg$ possible, whereas a box and a triangle can be constructed also with other initial states.

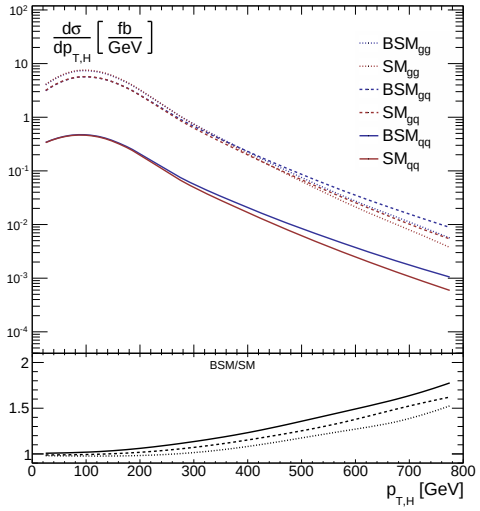

Figure 3.5: Parton–level $p_{T,H}$ distributions for Hjj production with the inital states qq (solid), gq (dashed) and gg (dotted). The red curves corresponds to the Standard Model $\kappa_{t,g} = (1, 0)$, while the blues curves follow from the BSM hypothesis $\kappa_{t,g} = (0.8, 0.2)$.

fore. This topology is only approximately implemented in the 1–jet matrix element, but is already correctly described by 2–jet matrix element. The pentagon loop does not seem to be dominant. Therefore a third jet would be most helpful as part of final state splitting, however this is can be reasonably well described by the parton shower and must not necessarily be part of the matrix element.

The logarithms depend dominantly on the transverse momentum of the jet or Higgs, so we expect no large difference between SM and BSM in other observables than p_T. In Fig. 3.6 we present some other exemplary distribution like the invariant mass of the dijet system. All curves are aligned, indicating that strong top mass effects are indeed only appearing in the transverse momentum spectra. We therefore have only those two observables to resolve the Higgs–gluon coupling.

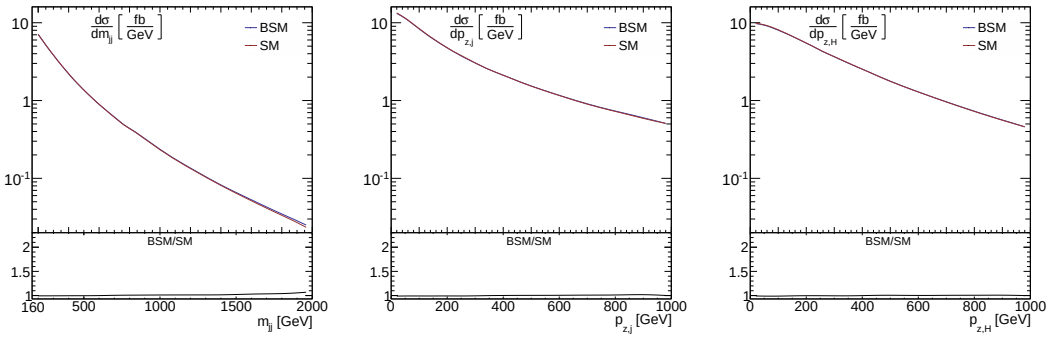

Figure 3.6: Parton–level m_{jj} (left), p_{z,j_1} (center) and $p_{z,H}$ (right) distributions for Hjj production.

3.2.3 Full Simulation

While all above observations are true at parton level, the question is if attaching a proper parton shower changes the picture. A parton shower simulates additional jet radiation attached to a matrix element and thus effects the shape of the p_T peak. Since this jet radiation is mainly soft we expect it to change only the low–p_T regime. We therefore showered both processes by running PYTHIA8 [91] over the previously with MCFM [70, 71] and VBFNLO [72–74] generated Les Houches Accord event samples [92]. For the renormalization and factorization scale we choosed $\mu_R^2 = \mu_F^2 = m_H^2 + p_{T,j}^2$ and $\mu_R^2 = \mu_F^2 = m_H^2 + p_{T,j1}^2 + p_{T,j2}^2$, respectively. For technical reason we included a decay of the Higgs to two taus, but its impact on the shape of the distribution is neglectable.

We present the results of a full simulation in Fig. 3.7 for the $p_{T,H}$ distribution in terms of the different contribution defined in Eq. (3.4). The interference curve is determined from the simulation of the Standard Model, the pure HEFT approximation and the BSM distribution, using

$$\frac{d\sigma_{tg}}{dp_{T,H}} = \frac{1}{2\kappa_t\kappa_g}\left(\frac{d\sigma_{\text{BSM}}}{dp_{T,H}} - \kappa_t^2\frac{d\sigma_{\text{SM}}}{dp_{T,H}} - \kappa_g^2\frac{d\sigma_{\text{HEFT}}}{dp_{T,H}}\right). \tag{3.10}$$

We see that even though the peak is broadened, the distributions still split up at approximately 300 GeV. For all three contributions defined in Eq. (3.4) the Hjj process is more dominant than the Hj process, as we have already seen in the parton level case. This is expected, because the parton shower does not only underestimates the radiation of boosted jets for the Hj process, but also cannot reflect the top mass logarithms. The higher rate for the 2–jet matrix element in the sensitive region is a good starting point for a signal–background analysis and even provides more handles to suppress the Standard Model backgrounds at the LHC.

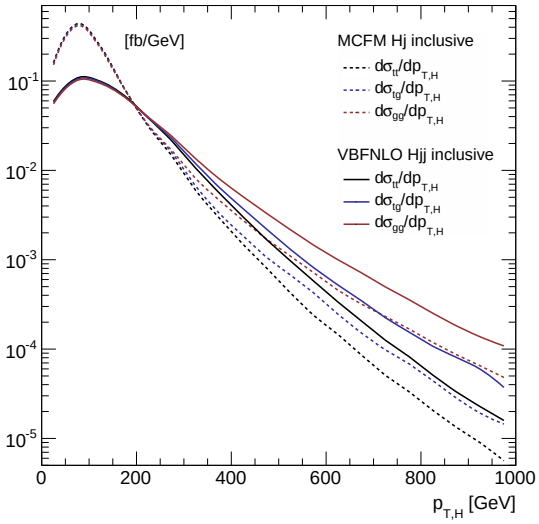

Figure 3.7: Transverse momentum distribution for Hj production (based on MCFM) and Hjj production (based on VBFNLO). Both codes use PYTHIA8 for the parton shower. The top–induced and dimension-6 contributions as well as their interference are defined in Eq. (3.4). We assume $\sqrt{s} = 13$ TeV and for technical reasons include a decay $H \to \tau\tau$ with minimal cuts.

3.3 Signal–Background Analyses

When looking for new physics it is not sufficient just to study the signal itself. Experimentally it defines a final state with which the signal events can be selected with the trigger system at the LHC, but the trigger also selects events which have a different origin. The number of those background events is in fact almost always larger then number of signal events. A careful analysis is then necessary to reduce the background and make a meaningful statistical analysis possible.

So far we have studied the signal in a general fashion and compared the Hj [51, 52, 87] with the Hjj process, keeping the Higgs stable. We will now focus on two of the most promising decay channels of the Higgs, $H \to WW$ and $H \to \tau\tau$. To select those events at the LHC we look in both channels for a leptonic final state with two opposite charged leptons. This excludes a hadronic W and tau decay, but we gain a final state signature which is easy to identify in a detector. Even though the leptonic decay of the W and the τ leads to undetectable neutrinos and therefore to difficulties in reconstructing the Higgs, this signature can be used to get background processes under control.

The major background processes for this final state are WW+jets and $t\bar{t}$+jets with leptonic decays. The Z/γ^*+jets process also accounts for the background, but its contribution can be brought to a minimal level in the phase space region of interest, as we will show in the $\tau\tau$ analysis. Feynman diagrams representing the signal and background processes are presented

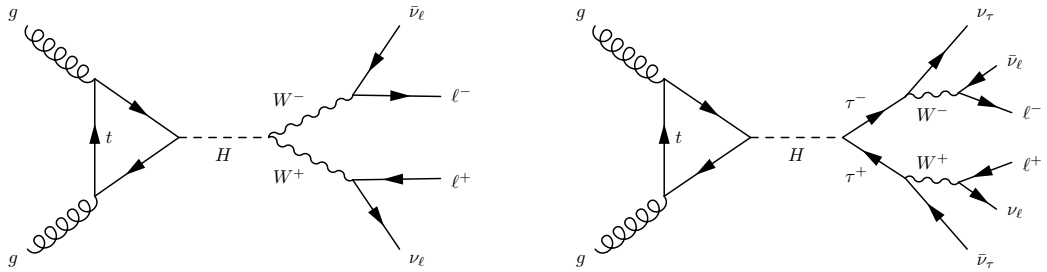

Figure 3.8: Sample Feynman diagrams for the two different decay channels $H \to WW$ (left) and $H \to \tau\tau$ (right) in gluon fusion with subsequent decays to a leptonic final state.

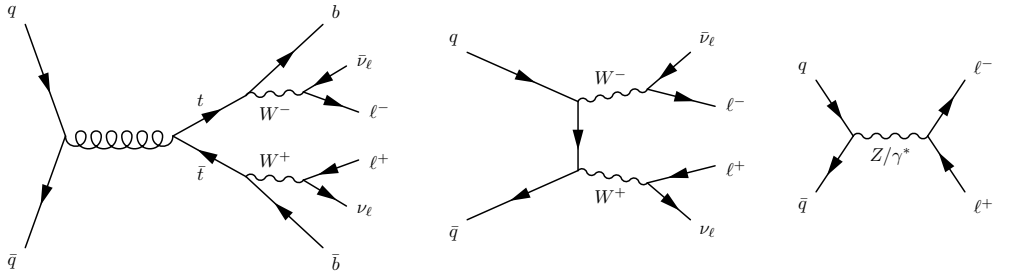

Figure 3.9: Sample Feynman diagrams for the corresponding background processes $t\bar{t}$ (left), WW (middle) and Z/γ^* (right).

in Fig. 3.8 and Fig. 3.9, respectively. Note that the ambition of the following analysis is not to give a realistic estimate for a measurement of κ_t and κ_g, but to see how the Hj and Hjj process compare in a basic LHC analysis at $\sqrt{s} = 13$ TeV.

As before, the signal events are generated with McfmPythia8 [70, 71, 91] for the Hj process and with VbfNloPythia8 [72–74, 91] for the Hjj process. Scale choices are $\mu_R^2 = \mu_F^2 = m_H^2 + p_{T,j}^2$ and $\mu_R^2 = \mu_F^2 = m_H^2 + p_{T,j1}^2 + p_{T,j2}^2$, respectively, and the PDF set is Cteq6l1 [75].

The WW and top backgrounds are generated at NLO with the PowhegBox [93, 94] and showered with a vetoed shower implemented in Pythia8. The vetoed shower prevents any shower emission with p_T greater than the Powheg emission [95], which is necessary to avoid double counting of jets. The PDF set Cteq6m [75] is used.

The Z/γ^*+jets background is generated at NLO with up to three jets in Sherpa [77–82] using the CT10 PDF set [96] and the build–in METS scale setter. For the NLO calculation within in the Mc@Nlo framework [97] Sherpa is interfaced with BlackHat [98].

The visible final state, excluding leptons and photons, are clustered to jets. For this purpose we used the anti–k_T algorithm implement in FastJet [99, 100] with a cone radius of $R = 0.5$. Jets are required to be sufficiently hard,

$$p_{T,j} > 40 \text{ GeV} \qquad \text{and} \qquad |y_j| < 4.5. \tag{3.11}$$

The cut on the rapidity of the jet corresponds to the typical experimental limit of a LHC

detector. If not otherwise mentioned we will refer to the leading and subleading jet as the two hardest jets fulfilling this requirement.

We apply similar criteria for the leptons,

$$p_{T,\ell} > 20 \text{ GeV} \qquad \text{and} \qquad |y_\ell| < 2.5, \tag{3.12}$$

where the rapidity range is reduced since leptons are detected in the electromagnetic rather than the hadronic calorimeter. Additionally leptons have to be isolated, *i.e.* the transverse hadronic energy deposit $E_{T,\text{had}} = \sum_{\text{vis}} p_T$ should not exceed $E_{T,\ell}/10$ within a cone around the lepton of radius $R = 0.2$. This reduces the amount of leptons which are not part of the hard process but created as part of a jet. Events which do not contain exactly two opposite sign leptons are vetoed.

In order to suppress the top background we require zero b-tagged jets due to the dominant $t \to bW$ decay. Experimentally identifying jets originating from b quarks is challenging and not foolproof, but a high efficiency is achieved in recent years [101]. Since we have in simulations full control over the jet origin we assumed a flat, *i.e.* energy independent, tagging efficiency of 70% and a light flavour mistag rate of 2%.

All so far mentioned selection criteria are applied to both Higgs decay channels and all backgrounds. To address the different decay signatures a different set of additional cuts is applied to both channels afterwards. They are described in the following Sec. 3.3.1 and 3.3.2, respectively and are similar to the known analysis techniques.

3.3.1 $H \to \tau\tau$ Decays

In the $H \to \tau\tau$ channel, both τ particles decay independently such that differently flavoured final state leptons are possible. In the large $Z \to \ell\ell$ background the leptons are created in pairs and are therefore of same flavour. Here, we expect a large amount of events where the invariant lepton mass $m_{\ell\ell}$ is around the Z mass of 91.2 GeV. Demanding $m_{\ell\ell} \in [10, 60]$ GeV for leptons of same flavour addresses this background by leaving out the Z–pole contribution. The minimal $m_{\ell\ell}$ requirement reduced the QED background, where the lepton pair is created by a γ^*. In case of differently flavoured leptons this cut can be opened to $m_{\ell\ell'} \in [10, 100]$ GeV. An even higher invariant mass window around the Higgs mass is not necessary since the four neutrinos from the tau decays lower the observed $m_{\ell\ell}$ of the final state leptons.

Even though we have all sort of stable leptons in the final state we are after a $\tau\tau$ signature. A leptonic tau decay involves two undetectable neutrinos, which leads to missing transverse energy/momentum $\not{E}_T$. We define $\not{E}_T$ as the absolute value of the negative vectorial sum over all visible transverse momenta and require it to exceed 45 GeV. In order to account for detector effects we smear the missing energy vector using a gaussian of width $-0.07 + 2.92$ GeV$/\not{E}_T$ before applying the cut.

A very efficient way to select the signal is to require the invariant tau mass $m_{\tau\tau}$ to be around the Higgs mass. However, $m_{\tau\tau}$ can not be exactly reconstructed, due to missing momentum. Instead we use the collinear approximation method [47], which assumes the neutrinos to be collinear with its corresponding lepton and that they are the only source of missing energy,

$$\begin{aligned} \not{E}_{T,x} &= |\vec{p}_{\text{miss},1}| \sin\theta_{\ell,1} \cos\phi_{\ell,1} + |\vec{p}_{\text{miss},2}| \sin\theta_{\ell,2} \cos\phi_{\ell,2} \\ \not{E}_{T,y} &= |\vec{p}_{\text{miss},1}| \sin\theta_{\ell,1} \sin\phi_{\ell,1} + |\vec{p}_{\text{miss},2}| \sin\theta_{\ell,2} \sin\phi_{\ell,2}. \end{aligned} \tag{3.13}$$

Solving this equation system leads to

$$\begin{aligned} |\vec{p}_{\text{miss},1}| &= \frac{\not{E}_{T,y} \cos\phi_{\ell,2} - \not{E}_{T,x} \sin\phi_{\ell,2}}{\sin\theta_{\ell,1} \sin(\phi_{\ell,1} - \phi_{\ell,2})} \\ |\vec{p}_{\text{miss},2}| &= -\frac{\not{E}_{T,y} \cos\phi_{\ell,1} - \not{E}_{T,x} \sin\phi_{\ell,1}}{\sin\theta_{\ell,2} \sin(\phi_{\ell,1} - \phi_{\ell,2})}. \end{aligned} \tag{3.14}$$

Using the momentum fraction x_i carried away by the lepton, the invariant tau mass can be calculated as

$$m_{\tau\tau} = \frac{m_{\ell\ell}}{\sqrt{x_1 x_2}} \qquad \text{with} \qquad x_i = \frac{|\vec{p}_{\ell,i}|}{|\vec{p}_{\ell,i}| + |\vec{p}_{\text{miss},i}|}. \tag{3.15}$$

This approximation works well in the boosted regime, but can lead to imaginary results for back–to–back leptons due to $|\vec{p}_{\text{miss},i}| \propto \sin(\phi_{\ell,1} - \phi_{\ell,2})^{-1}$. We therefore require

$$|m_{\tau\tau} - m_H| < 20 \text{ GeV} \qquad \text{with} \qquad x_i \in [0.1, 1] \tag{3.16}$$

and to ensure that we fulfil the kinematical conditions for the collinear approximation

$$p_{T,H} \sim \left| \vec{p}_{T,\ell_1} + \vec{p}_{T,\ell_2} + \vec{\not{E}}_T \right| > 300 \text{ GeV}. \tag{3.17}$$

The large mass window around m_H should include most of the signal events, while we see in Tab. 3.1 that only a fraction of the background events fulfill this requirement.

Those new cuts do not require any jet since we have used the common single jet observables already in our bare cuts. However, we can make use of the second jet by defining additional 2–jet correlation observables in order to suppress the background even further. This, of course, only make sense applying to the Hjj process.

In turns out that the difference in azimuthal angle $\Delta\phi_{jj}$ between the two tagging jets [102–109], as well as the ratio of transverse momenta $p_{T,j1}/p_{T,j2}$, are performing well. In Fig. 3.10 we show the normalized corresponding distributions after applying all so far mentioned selection criteria. Especially the $t\bar{t}$ background can be reduced by cutting on those two 2–jet observables. In the boosted Higgs regime the preferred kinematical configuration are two balanced jets recoiling against the Higgs. They are close together in the azimuthal plane. This shows again that two hard jets are of advantage and that the Hjj matrix element is of

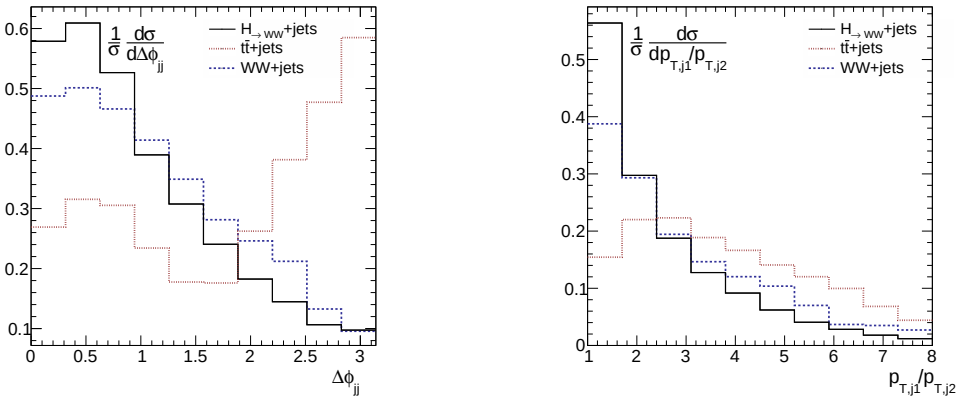

Figure 3.10: Normalized $\Delta\phi_{jj}$ (left) and $p_{T,j1}/p_{T,j2}$ (right) distributions for the $H \to \tau\tau$ signal and the dominant backgrounds. All universal cuts listed in Tab. 3.1 are already applied.

	$Hj \to (\tau\tau)j$ inclusive				$Hjj \to (\tau\tau)jj$ inclusive			
cuts	H+jets	Z/γ^*+jets	WW+jets	$t\bar{t}$+jets	H+jets	Z/γ^*+jets	WW+jets	$t\bar{t}$+jets
$p_{T,j} > 40$ GeV, $\lvert y_j\rvert < 4.5$ $p_{T,\ell} > 20$ GeV, $\lvert y_\ell\rvert < 2.5$	9.82	162303	524	14770	5.10	27670	90.7	7633
$N_b = 0$	9.21	148221	515	4920	4.50	23218	87.4	1690
$m_{\ell\ell} \in [10, 60]$ GeV $m_{\ell\ell'} \in [10, 100]$ GeV	6.59	10466	179	1616	3.41	1832	28.3	541
$\not{E}_T > 45$ GeV	6.24	38.1	166	1616	3.31	0.65	27.0	541
$\lvert m_{\tau\tau} - m_H\rvert < 20$ GeV	5.88	2.84	6.28	45.9	3.10	0.11	1.18	16.0
$p_{T,H} > 300$ GeV	0.23	0.013	0.40	0.87	0.41	0.004	0.20	0.56
$\Delta\phi_{jj} < 1.8$					0.33	0	0.15	0.22
$p_{T,j1}/p_{T,j2} < 2.5$					0.22	0	0.076	0.086

Table 3.1: Cut flow for H+jets, Z/γ^*+jets, WW+jets and $t\bar{t}$+jets. All rates are given in fb.

importance. We require

$$\Delta\phi_{jj} < 1.8 \qquad \text{and} \qquad \frac{p_{T,j1}}{p_{T,j2}} < 2.5. \tag{3.18}$$

Obviously, we do not apply a cut on m_{jj}, like it is done in many Higgs plus two jet analyses. This cut works well for a weak boson fusion characteristic, where the jets favour the forward–backward topology. This is due to a missing colour–flow between the in– and outcoming partons, however, this is not true for the Higgs produced in gluon fusion we are targeting. Beside reducing the signal itself, a cut on m_{jj} would also not enhance the BSM component, as we have seen in Fig. 3.6.

To compare the Hj [51, 52, 87] and Hjj process we get the 1–jet inclusive and 2–jet inclusive samples from simulation based on the 1–jet matrix element and 2–jet matrix element, respectively. The corresponding cut–flow is presented in Tab. 3.1 for signal and background. We see that after applying all selection criteria the Hj and Hjj signal is of similar size in the sensitive region, but the backgrounds contributions are smaller by almost a factor of 8 in the 2–jet inclusive case. The S/B ratio is 0.2 and 1.4, respectively.

To finally extract information about the parameters κ_g and κ_t from these event samples, we performed a statistical shape analysis. This procedure is described in Sec. 3.3.3.

3.3.2 $H \to WW$ Decays

For the $H \to WW$ decay channel we start with cuts similar to those of the $H \to \tau\tau$ channel. Due to the subsequent decay $W \to \ell\nu$ we require the invariant lepton mass to be between 10 GeV and 60 GeV, as well as missing transverse momenta $\not{E}_T$ of at least 45 GeV. We also employed a cut on the difference in azimuthal angle of the two leptons,

$$\Delta\phi_{\ell\ell} < 1.8. \tag{3.19}$$

Looking at the cut–flow in Tab. 3.2, this cut on the angular correlation seems not to be very efficient, as it suppresses the signal almost as much as the backgrounds. However, we have to keep in mind that the sensitive region is the boosted Higgs regime and in this region it turns out the cut does serve its purpose.

A very effective way to reduce background is to cut on the transverse mass m_T. In the WW system with leptonic decays it is defined as

$$m_T^2 = (E_T^{\ell\ell} + \not{E}_T)^2 - |\vec{p}_T^{\,\ell\ell} + \vec{\not{E}}_T|^2 \qquad \text{with} \qquad E_T^{\ell\ell} = \sqrt{|\vec{p}_T^{\,\ell\ell}|^2 + m_{\ell\ell}^2}\,. \tag{3.20}$$

The important characteristic of this mass is, that it can not exceed the mass of the original mother particle. For the signal this means $m_T \leq m_H$, whereas in case of a different production mechanism larger values are possible. Therefore we require the transverse mass to be smaller than $m_H = 125$ GeV. We lose very little signal, but some background.

Like in the $\tau\tau$ channel we use

$$p_{T,H} \sim \left|\vec{p}_{T,\ell_1} + \vec{p}_{T,\ell_2} + \vec{\not{E}}_T\right| > 300 \text{ GeV} \tag{3.21}$$

to go into the region of interest. As indicated by Fig. 3.11, the 2–jet observables $p_{T,j1}/p_{T,j2}$ and $\Delta\phi_{jj}$ are also in this channel useful to suppress the background. We employ the same cut values for the Hjj process,

$$\Delta\phi_{jj} < 1.8 \qquad \text{and} \qquad \frac{p_{T,j1}}{p_{T,j2}} < 2.5. \tag{3.22}$$

As shown in Tab. 3.2, we have a similar picture when we compare the Hj with the Hjj process as in the $\tau\tau$ analysis. The size of the signal is comparable in the boosted regime but the signal–to–background ratio S/B is better by a factor of 7. For the Hjj process the background is roughly a factor of 2 larger than the signal. A statistical analysis in terms of an event shape analysis is presented in the following section for both decay channels of the Higgs.

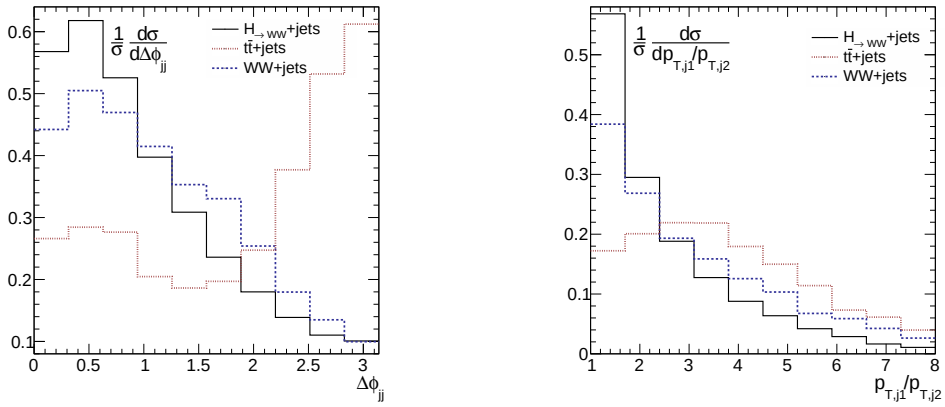

Figure 3.11: Normalized $\Delta\phi_{jj}$ (left) and $p_{T,j1}/p_{T,j2}$ (right) distributions for the $H \to WW$ signal and the dominant backgrounds. All universal cuts listed in Tab. 3.2 are already applied.

	$Hj \to (WW)j$ inclusive			$Hjj \to (WW)jj$ inclusive		
cuts	H+jets	WW+jets	$t\bar{t}$+jets	H+jets	WW+jets	$t\bar{t}$+jets
$p_{T,j} > 40$ GeV, $\lvert y_j\rvert < 4.5$ $p_{T,\ell} > 20$ GeV, $\lvert y_\ell\rvert < 2.5$	35.5	524	14770	17.3	90.7	7633
$N_b = 0$	33.3	515	4920	15.2	87.4	1690
$m_{\ell\ell} \in [10, 60]$ GeV	28.3	106	1060	13.0	17.2	351
$\not{E}_T > 45$ GeV	21.4	92.9	930	10.6	15.9	309
$\Delta\phi_{\ell\ell} < 0.8$	14.3	49.8	479	8.14	10.3	162
$m_T < 125$ GeV	14.2	26.6	220	8.09	6.14	76.2
$p_{T,H} > 300$ GeV	0.59	2.73	5.18	1.06	1.39	3.28
$\Delta\phi_{jj} < 1.8$				0.87	1.05	1.33
$p_{T,j1}/p_{T,j2} < 2.5$				0.57	0.53	0.53

Table 3.2: Cut flow for H+jets, WW+jets and $t\bar{t}$+jets. All rates are given in fb.

3.3.3 Shape Analysis

As we have seen, we get a difference between the BSM and SM hypothesis in the transverse spectra of the leading jet and the Higgs. Thus we can extract information about the parameters κ_g and κ_t when looking at the shape of this distributions. We therefore perform a shape analysis using the $p_{T,H}$ and $p_{T,j}$ distribution of the $H \to \tau\tau$ and $H \to WW$ channel described in the last two sections. We are focusing on the Hjj process, since the number of expected events is comparable to the Hj process, but its signal–to–background ratio is better.

We used the CL_s method, described in Sec. 2.3, to get exclusion limits for the parameter set $(\kappa_t, \kappa_g)_{\mathrm{BSM}} = (0.7, 0.3)$. The implementation of choice for this purpose was McLimit [110–112] within Root [76]. The Standard Model is defined to be the null hypothesis and the relevant backgrounds are included. The differential cross sections are translated into total event numbers by multiplying with the integrated luminosity. Even though we get the most sensitivity out of the boosted regime, we have skipped the cut on $p_{T,H}$ to get a the most out

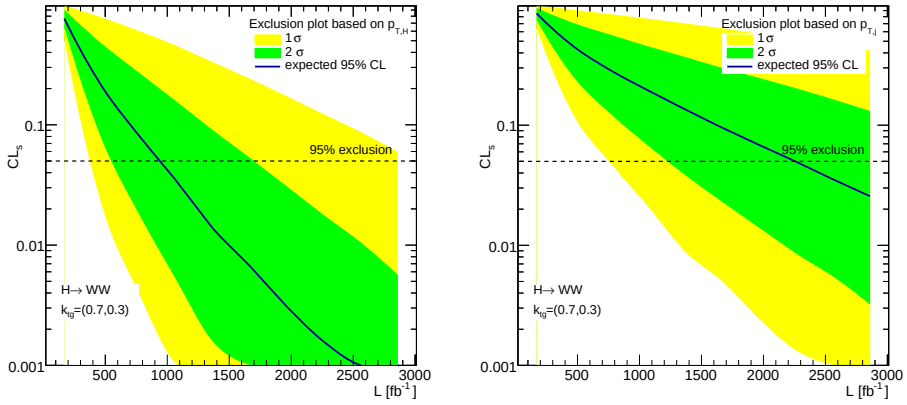

Figure 3.12: Confidence level for separating the BSM hypotheses $\kappa_{t,g} = (0.7, 0.3)$ from the Standard Model. We show results for $H \to WW$ decays based on the transverse momentum of the Higgs (left) and the hardest jet (right).

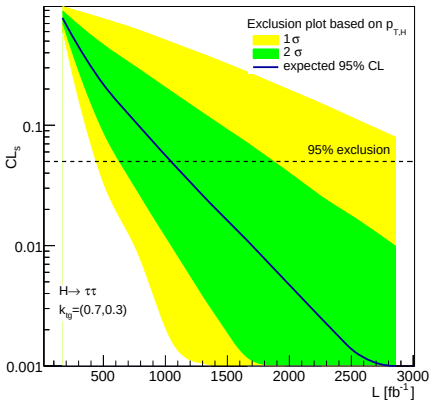

Figure 3.13: Confidence level for separating the BSM hypotheses $\kappa_{t,g} = (0.7, 0.3)$ from the Standard Model. We show results for the $H \to \tau\tau$ decays. We limit ourselves to the more promising case of the Higgs transverse momentum.

of the shape. In order to account for the NLO scale choice we assumed a scale uncertainty of $\mathcal{O}(20\%)$ [72–74].

In Fig. 3.12 and Fig. 3.13 we show the confidence level for a given integrated luminosity, based on the $p_{T,H}$ distribution for both decay channels respectively. The $\pm 1\sigma$ and $\pm 2\sigma$ uncertainty bands are presented in green and yellow respectively. We also show a confidence level plot based on $p_{T,j}$ for the WW channel, but we clearly see that the transverse mass of the Higgs seems to be better suited. Even though the WW signal has a higher cross section than the $\tau\tau$ signal, its signal–to–background ratio is worse. After all we find that the WW and $\tau\tau$ decay channel are performing similarly well.

3.4 Extension to NLO Merging

As we have seen, the Hjj process has a higher cross section in the top mass sensitive boosted Higgs regime. This makes the process numerically an important contribution when resolving the Higgs–gluon coupling. Since a signal–background analysis also benefits from the second hard jet the Hjj process can not be seen just as a correction to the Hj process. However, both processes show a similar logarithmic structure, thus it is a natural extension to combine both matrix elements to get the most out of it.

This section presents the result when repeating our analysis with state of the art event samples which merges the H, Hj and Hjj processes. Additionally the hard processes H and HJ are calculated and merged at NLO. The Hjj contribution remains at LO. For this purpose we got access to developmental implementations in SHERPA+OPENLOOPS [77–83]. Given that $p_{T,H}$ is an inclusive observable we expect not only a better estimate of the differential cross section over the full momentum range when using multi–jet merged samples, but also better new physics constraints.

3.4.1 Multi–Jet Merging at LO

First, we want to focus in multi–jet merging, before introducing NLO corrections. In order to verify our results we used two independent sets of tools to obtain LO event samples.

On the one hand we used SHERPA [77–82] to obtain CKKW–merged [113] event samples. This relies on the low–energy limit of the Higgs–gluon coupling thus all tree–level matrix elements are reweighted with their full loop counterpart for each jet multiplicity n by

$$r^{(n)} = \frac{\left|\mathcal{M}^{(n)}(m_t)\right|^2}{\left|\mathcal{M}^{(n)}(m_t \to \infty)\right|^2}. \tag{3.23}$$

On the other hand we used events showered by PYTHIA8 [91] and merged via the CKKW–L algorithm [114]. The 0–jet parton level events were generated with MADGRAPH5 [115], the 1–jet with MCFM [70, 71] and the 2–jet events with VBFNLO [72–74]. All tools use the same LO PDF set CTEQ6L1 [75] in order to compare them.

As we have seen in the previous section we obtain from the WW and $\tau\tau$ decay channel similar exclusion limits, we therefore focus only on the $WW \to \ell\nu\ell\nu$ decay. We define a jet via the anti–k_T algorithm using FASTJET [99, 100] with a cone radius of 0.4. Our basic acceptance cuts are

$$\begin{aligned} p_{T,\ell} &> 20 \text{ GeV}, \qquad |\eta_\ell| < 2.5, \\ p_{T,j} &> 30 \text{ GeV}, \qquad |\eta_j| < 2.4 \end{aligned} \tag{3.24}$$

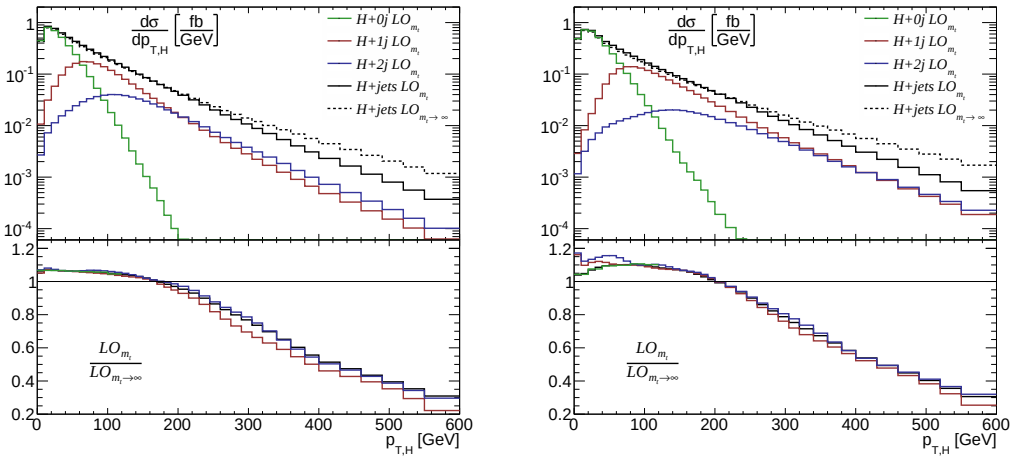

Figure 3.14: Transverse momentum distribution $p_{T,H}$ for $H \to WW$+jets production at LO with SHERPA (left panel) and PYTHIA8 (right panel). We present the distributions for exclusive and merged jet samples with finite top mass effects ($m_t = 173$ GeV) and in the low-energy approximation ($m_t \to \infty$). We assume the LHC at $\sqrt{s} = 13$ TeV.

and we reconstruct the transverse momentum of the Higgs via

$$p_{T,H} \sim \left| \vec{p}_{T,\ell_1} + \vec{p}_{T,\ell_2} + \not{\vec{E}}_T \right| . \tag{3.25}$$

The missing transverse energy vector is, as before, smeared with a gaussian.

We present the results in Fig. 3.14. The individual jet–bins shown in this figure correspond to the number of jets passing our acceptance cuts. Both results from SHERPA and PYTHIA8 agree with each other in the boosted regime.

We see that in the low–energy regime we get a constant scaling factor of about 1.065 for SHERPA between the full top mass dependence and the HEFT approximation. This factor is universal for all jet bins. The PYTHIA8 simulation shows some slight discrepancies in the low–p_T regime. The ratios in each jet–bin do not factorize and are not constant. This is a remnant of the merging procedure in PYTHIA8.

Above around 300 GeV the two hypotheses split up, as we have seen before, reaching a difference in rate of four at 600 GeV. It is an interesting observation that the top mass effects factorize, *i.e* we get the same correction for all jet bins, thus also for the merged results. This is another indication that the top mass effects are indeed fully associated to the hard process. In fact, this is only true for top mass effects, whereas it is known it does not apply to bottom mass effects.But as we already mentioned bottom mass effects do not play an important role in the boosted regime. It is worth mentioning that in the merged event sample the 2–jet subsample has still a higher rate in the boosted regime than the 1–jet subsample. Therefore the basic picture of our previous analysis did not change.

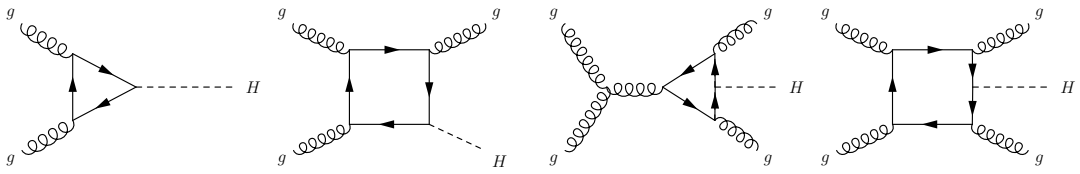

Figure 3.15: Sample of the Feynman diagrams contributing for Higgs production with up to 2 jets at leading order.

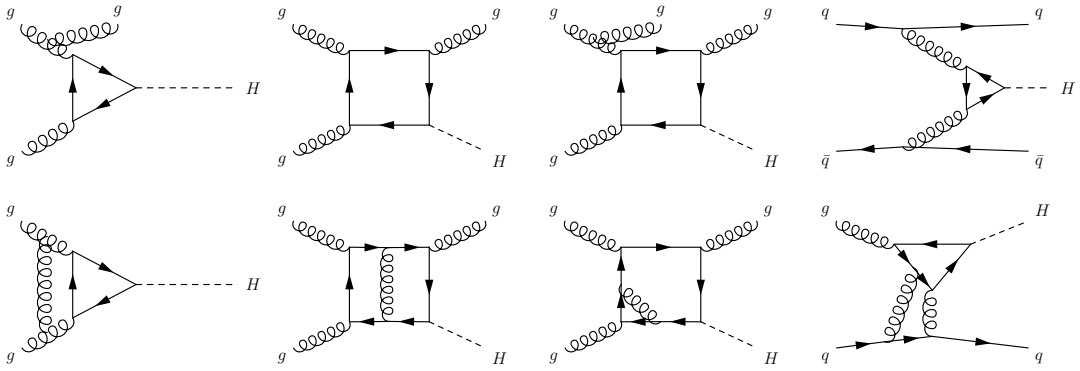

Figure 3.16: Sample of the one-loop Feynman diagrams contributing to the Higgs and Higgs-jet production. On the top we display the NLO real corrections and on the bottom the virtual contributions.

3.4.2 Multi–Jet Merging at NLO

After we have discussed the effect of multi–jet merging on rates and top mass effects we can now additionally add NLO corrections. They will significantly increase the total rate, but we will also have a look at the shape of the p_T distribution and its influence on the ratio between the Standard Model and HEFT approximation.

The structure of a NLO cross section can be written for illustrational purposes as

$$d\sigma_{\mathrm{NLO}} = (\mathcal{B} + \mathcal{V} + \mathcal{I})\, d\Phi_n + (\mathcal{R} - \mathcal{D})\, d\Phi_{n+1} \tag{3.26}$$

$\mathcal{B}$ is the Born term and corresponds to the leading order part of the cross section. Sample Feynman diagrams for different jet multiplicities can be found in Fig. 3.15. $\mathcal{V}$ is the virutal term which comprise all virtual corrections to the LO process. $\mathcal{R}$ denotes the real corrections where one extra final state parton is added to the process. Sample Feynman diagrams for virtual and real corrections can be found in Fig. 3.16. $\mathcal{I}$ and $\mathcal{D}$ are the integrated and unintegrated dipole subtraction term, which is introduced in order to cancel unphysical divergencies. $d\Phi_n$ and $d\Phi_{n+1}$ are the n and $n+1$ phase space integrals.

The samples present in this section are based on 0–jet and 1–jet events at NLO and 2–jet events at LO. They are generated with Sherpa and merged using the Meps@Nlo algo-

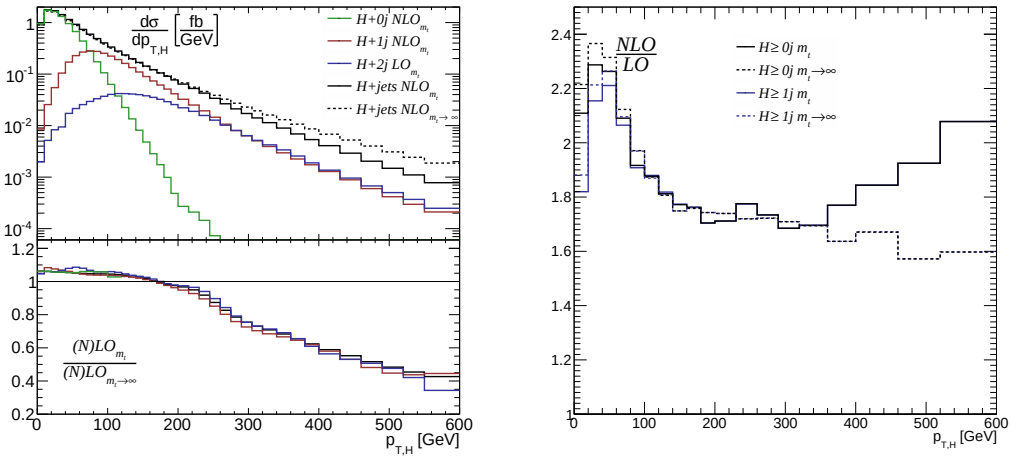

Figure 3.17: Transverse momentum distribution $p_{T,H}$ for $H \to WW$+jets production with SHERPA at NLO (left panel) and correspondent NLO K-factor for each jet multiplicity (right panel). We present the distributions for exclusive and merged jet samples with finite top mass effects ($m_t = 173$ GeV) and in the HEFT approximation ($m_t \to \infty$). Both plots are still preliminary.

rithm [116].The top (and bottom) mass effects at leading order accuracy are included by using matrix elements provided by OPENLOOPS [83]. All plots are still preliminary, however we do not expect them to change significantly.

In the left panel of Fig. 3.17 we see that the total rate is enhanced in comparison to the LO simulation in Fig. 3.14. The 2–jet subsample seems to have lost some significance, but this is due to the fact that the 2–jet matrix elements remain at LO, whereas the 1–jet is already at NLO accuracy. The top mass effects still factorize in each jet bin and converge to a constant factor in the low–energy regime.

The right panel of Fig. 3.17 shows the K–factor due to NLO corrections. We can see, that the correction factor depends on p_T and is roughly around 2. Interestingly, we get a different K–factor for the Standard Model scenario and the pure dimension–6 hypothesis in the boosted regime. Because the NLO corrections in this regime appear to be less for the dimension–6 scenario than the loop–induced Standard Model, the difference between both scenarios is slightly reduced at NLO.

Nevertheless, those two plots show impressively that in order to simulate the p_T spectra accurately, both corrections are vital. While the NLO corrections increase the rate by roughly a factor of 2 especially for low energies, top mass effects change the rate in the boosted regime massively.

4 Off–Shell Higgs Production

4.1 Framework

In the previous chapter we saw that for the investigated processes top mass effects are present in the boosted Higgs regime. As for most Higgs property measurements the information where dominantly extracted from a Higgs produced on its mass shell. Only recently the off-shell regime in the $pp \to Z^{(*)}Z^{(*)} \to 4\ell$ was explored by the CMS and ATLAS collaboration [56–58]. This process includes a s–channel $gg \to H \to ZZ$ process, which interfere with the loop–induced $gg \to ZZ$ continuums background. The complete ZZ production via two gluons therefore inherits information about the Higgs and its coupling to gluons. Illustrative Feynman diagrams can be found in Fig. 4.1.

The major background contribution to the Higgs signal comes from $q\bar{q} \to ZZ$, since it is the only tree–level process. It is followed by the $gg \to ZZ$ continuums production. The overall off-shell contribution gets sizable when the ZZ on-shell threshold is reached [53–55, 117]. While this channel was studied mainly for Higgs width measurements [53–57], we want to see if we can extract top mass effects originating from the Higgs–gluon coupling. Later on we will also comment in Higgs width measurements, which can be related to dimension–6 operators [118].

As pointed out in [59, 60], a different kind of logarithm arises for some helicity amplitudes in the $gg \to H \to ZZ$ channel, *e.g.*

$$\mathcal{M}_{ZZ}^{++00} \propto \log^2\left(\frac{m_{4\ell}^2}{m_t^2}\right). \tag{4.1}$$

This is our main motivation for looking at off-shell Higgs production, because away from an on-shell produced Higgs with $m_{4\ell} \approx m_H$, we expect top mass effects in this regime. We therefore exploit this process in a similar way as we did for the top mass effects in boosted Higgs production and work out the impact of this new logarithmic structure. The only major difference is that we are now interested in the differential distribution of the invariant mass of the lepton system instead of the transverse momentum. We will discuss this logarithmic structure further in Sec. 4.2.1.

The basic framework is the same as for the boosted Higgs in the previous chapter, *i.e.* the parameterization of Eq. (3.1) still holds. This allows us to directly compare boosted and off-shell regime. However, in this channel it is important to include the interference of the

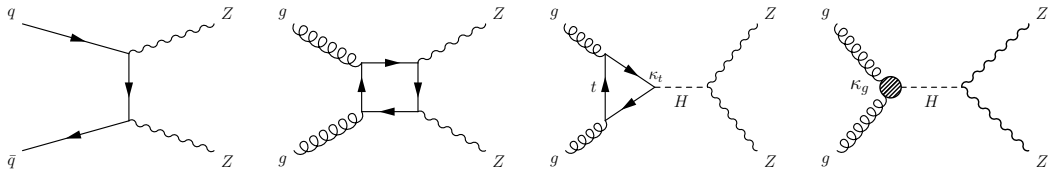

Figure 4.1: Sample of the Feynman diagrams for the continuum background $q\bar{q}\,(gg) \to ZZ$ (left) and for the signal $gg \to H \to ZZ$ (right) with full top mass dependence and in the $m_t \to \infty$ approximation.

signal with the $gg \to ZZ$ continuum background. We therefore need to add the corresponding background amplitude $\mathcal{M}_c$ to the matrix element

$$\mathcal{M}_{ZZ} = \kappa_t \mathcal{M}_t + \kappa_g \mathcal{M}_g + \mathcal{M}_c. \tag{4.2}$$

instead of disentangling background and signal. With the parameters κ_t and κ_g we can switch on different contributions. Again $k_{(t,g)} = (1, 0)$ corresponds to the Standard Model with top–loop induced Higgs–gluon coupling, whereas $k_{(t,g)} = (0, 1)$ is the pure dimension–6 scenario. Both include the gg background and interference. The continuums background alone is represented by the parameters $k_{(t,g)} = (0, 0)$.

Even though the corresponding expression in terms of differential cross sections for an observable operator $\mathcal{O}$ is now more lengthy than before,

$$\frac{d\sigma}{d\mathcal{O}} = \frac{d\sigma_{cc}}{d\mathcal{O}} + \kappa_t \frac{d\sigma_{tc}}{d\mathcal{O}} + \kappa_g \frac{d\sigma_{gc}}{d\mathcal{O}} + \kappa_t^2 \frac{d\sigma_{tt}}{d\mathcal{O}} + \kappa_t \kappa_g \frac{d\sigma_{tg}}{d\mathcal{O}} + \kappa_g^2 \frac{d\sigma_{gg}}{d\mathcal{O}}, \tag{4.3}$$

we gain from the additional interference term. Especially when the pure signal components proportional to κ_t^2 and $\kappa_t \kappa_g$ are small, the interference term proportional to κ_t and κ_g will be the dominant term which still carries information about the Higgs–gluon coupling.

4.2 Top Mass Effects

4.2.1 Logarithmic Structure

We already quoted in Eq. (4.1) that similar to the boosted Higgs regime a top mass dependent logarithm occurs. However, due to the interference with the background there is event more to say about this matrix element. At high invariant masses the Higgs decays dominantly into longitudinal gauge bosons. It is therefore sufficient to study only the longitudinal components, which for the helicity component $\mathcal{M}_t^{++00}$ and full top mass dependence can be written as [59, 60, 119]

$$\mathcal{M}_t^{++00} = -2 \frac{m_t^2}{m_Z^2} \frac{m_{4\ell}^2 - 2m_Z^2}{m_{4\ell}^2 - m_H^2 + i\Gamma_H m_H} \left[1 + (1 - \tau^*)\, f(\tau^*)\right]. \tag{4.4}$$

where Γ_H the Higgs boson width. The parameter τ^* and scalar three–point function $f(\tau^*)$ are defined as the off–shell analogue to τ and $f(\tau)$ in Eq. (2.22) and Eq. (2.23),

$$f(\tau^*) = -\frac{m_{4\ell}^2}{2} C(0,0,m_{4\ell}^2,m_t^2,m_t^2,m_t^2) = \begin{cases} \arcsin^2 \sqrt{\frac{1}{\tau^*}} & \text{for } \tau^* > 1 \\ -\frac{1}{4}\left[\ln\left(\frac{1+\sqrt{1-\tau^*}}{1-\sqrt{1-\tau^*}}\right) - i\pi\right]^2 & \text{for } \tau^* < 1 \end{cases}$$

$$\tau^* = 4\frac{m_t^2}{m_{4\ell}^2}. \tag{4.5}$$

Note that by essentially replacing m_H by its effective off-shell mass $m_{4\ell}$ we need to expand $f(\tau)$ for $\tau < 1$. This leads to two different scaling behaviours depending on the size of the invariant mass relative to $2m_t$.

We can express the above matrix–element in the far off–shell limit $m_{4\ell} \gg m_H, m_Z$ and for the two hypotheses with full top mass dependence $\tau^* \to 0$ and without $\tau^* \to \infty$,

$$\begin{aligned} \mathcal{M}_t^{++00} &\approx +\frac{m_t^2}{2m_Z^2} \ln^2\left(\frac{m_{4\ell}^2}{m_t^2}\right) \qquad \text{with} \qquad \tau^* \to 0, \quad m_{4\ell} \gg m_H, m_Z \\ \mathcal{M}_g^{++00} &\approx -\frac{m_{4\ell}^2}{2m_Z^2} \qquad\qquad\qquad\quad \text{with} \qquad \tau^* \to \infty, \quad m_{4\ell} \gg m_H, m_Z. \end{aligned} \tag{4.6}$$

Here we keep only the leading terms. $\mathcal{M}_t^{++00}$ corresponds therefore to the loop–induced Higgs–gluon coupling and $\mathcal{M}_g^{++00}$ to the pure dimension–6 Higgs–gluon coupling, both in the far off-shell regime. We see in these two approximations not only the occurrence and absence of the top dependent logarithm, but note also the difference in sign. Together with the matrix element for the continuums background in the high invariant mass limit

$$\mathcal{M}_c^{++00} \approx -\frac{m_t^2}{2m_Z^2} \ln^2\left(\frac{m_{4\ell}^2}{m_t^2}\right) \tag{4.7}$$

we conclude a overall negative sign of the interference term for the top mass dependent case and a positive sign for $m_t \to \infty$. Hence, we get a destructive and constructive interference between the signal and the continuums background in the high–$m_{4\ell}$ regime, respectively. For the correct theory with top mass dependence the logarithms cancel between $gg \to H \to ZZ$ and $gg \to ZZ$, ensuring a proper ultraviolet behaviour of the amplitude.

4.2.2 Parton Level Simulation

In order to see how strong the top mass effects are we simulate the different $gg \to ZZ \to 4\ell$ contributions at LO, as well as the purely by quarks initiated background at NLO. We used a $e^+e^-\mu^+\mu^-$ final state generated with MCFM-6.8 [70, 71] at a center of mass energy of $\sqrt{s} = 13$ TeV. The renormalisation and factorisation scale is set to $m_{4\ell}/2$ and the PDF set CTEQ6L1 [75] is used. To switch between the different gg initiated components the MCFM

code was modified and verified against an independent implementation in SHERPA [77–82].

Even though the $gg \to ZZ$ continuum process is currently only known at LO, the signal process $gg \to H \to ZZ$ is calculated to very high precision. Theoretical predictions for the gluon–fusion Higgs production are available at next–to–next–to–leading order (NNLO) and next–to–next–to–leading logarithm (NNLL) for inclusive production and at NNLO differentially as a function of m_{ZZ} [120]. It was shown recently, that NLO and NNLO corrections to the signal–background interference are quite similar to those of the signal. It was therefore concluded that one can use an equal K–factor for the gg components [121]. In order to account for missing the missing NLO corrections to the gg initiated components in our simulation we multiplied the differential distributions with this K–factor.

For event selection we followed the basic CMS off–shell cut–flow analysis [58]. We require

$$\begin{aligned} p_{T,e} &> 7 \text{ GeV}, \qquad |\eta_e| < 2.5, \\ p_{T,\mu} &> 5 \text{ GeV}, \qquad |\eta_\mu| < 2.4, \\ p_{T,\text{leading}} &> 20 \text{ GeV}, \\ p_{T,\text{subleading}} &> 10 \text{ GeV}, \end{aligned} \tag{4.8}$$

where (sub)leading corresponds to leptons ordered in p_T. Additionally

$$m_{\ell\ell'} > 4 \text{ GeV} \qquad \text{and} \qquad m_{4\ell} > 100 \text{ GeV} \tag{4.9}$$

must hold, where $m_{\ell\ell'}$ includes all lepton combinations independent of flavour. For the invariant masses $m_{\ell\ell}$ of same flavoured lepton pairs we demand

$$40 \text{ GeV} < m_{\ell\ell}^{\text{closest}} < 120 \text{ GeV} \tag{4.10}$$

for the pair closest to the Z mass and

$$12 \text{ GeV} < m_{\ell\ell}^{\text{furthest}} < 120 \text{ GeV} \tag{4.11}$$

for the other.

In the left panel of Fig. 4.2 we present parton level simulations of the $qq \to ZZ$ and $gg \to ZZ$ backgrounds without Higgs contributions, as well as the full gg initiated contribution including the interference of $gg \to H \to ZZ$ with the continuums background. We also show the corresponding ratio between top mass dependent gg component $k_{(t,g)} = (1, 0)$ and the gg component in its low–energy form $k_{(t,g)} = (0, 1)$. The right panel of Fig. 4.2 presents the pure $gg \to H \to ZZ$ component without the background interference. Also here we show the ratio between the Standard Model hypothesis $k_{(t,g)} = (1, 0)$ and the pure dimension–6 hypothesis $k_{(t,g)} = (0, 1)$.

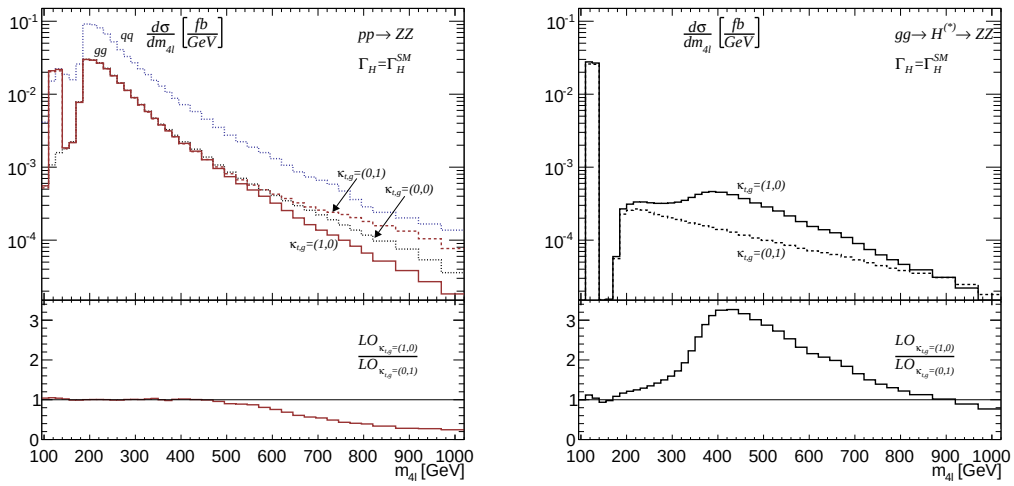

Figure 4.2: $m_{4\ell}$ distributions for the $gg \to ZZ$ (left) and $gg \to H \to ZZ$ (right) for the different signal hypothesis and the dominant background. We assume the LHC at $\sqrt{s} = 13$ TeV.

The shape of the distributions are largely dominated by threshold effects. If for instance some denominators in a scalar integral like the one in Eq. (2.24) vanish, the $i\epsilon$ prescription of the propagators become important. The matrix element then develops an absorptive imaginary contribution to the usually purely real part. Following the Cutkosky cutting rule [122], this happens for the scalar integral when replacing the internal propagators

$$1/\left(q^2 - m^2 + i\epsilon\right) \to 2\pi i\delta\left(q^2 - m^2\right). \tag{4.12}$$

This essentially we cut through every diagrams in all possible ways. If all affected internal propagators are simultaneously satisfying the on–shell condition we get an cross section enhancement.

One possible set of cuts are presented in Fig. 4.3 for the loop–induced $gg \to H \to ZZ$ process. The middle cut represents the narrow on–shell production resonance of the Higgs. The resonance peak is clearly visible in the right panel of Fig. 4.2 at around 125 GeV.

The right cut is the ZZ threshold at $2m_Z \approx 180$ GeV. When this threshold is reached the cross section is massively enhanced in all $pp \to ZZ$ contribution. This is numerically important, as an off–shell measurement would not be possible otherwise. The off–shell cross section would be just too small.

In the loop–induced signal another cut through the top loop is possible. This threshold is reached when both tops are simultaneously on–shell at around $2m_t = 340GeV$. This effect particularly visible in the right panel of Fig. 4.2 when comparing the Standard Model hypothesis with the pure dimension–6 scenario. While the Standard Model is indeed enhanced at around $2m_t$, the dimension–6 coupling does not inherit information about the top loop. It

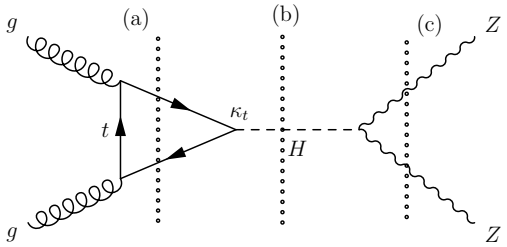

Figure 4.3: Representation of three different cuts through the Standard Model signal. If all cut propagators are on–shell the cross section is enhanced. (a) Top threshold around $2m_t$, (b) Higgs on–shell resonance at m_H and (c) ZZ threshold around $2m_Z$.

is not possible to cut through any top propagators and therefore this distribution does not show an enhancement. The corresponding ratio panel indicates a factor of 3 difference in cross section between both hypotheses.

If, however, also the gg continuum background and its interference is taken into account the top threshold enhancement is no longer dominant. This is shown in the left panel Fig. 4.2. Therefore the top threshold enhancement as an additional top mass effect to the top dependent logarithms will not lead to more sensitivity in resolving the Higgs–gluon coupling. After all the situation is similar to the boosted Higgs production and we rely on the logarithmic structure.

We see that the two hypotheses $k_{(t,g)} = (1, 0)$ and $k_{(t,g)} = (0, 1)$ split up for around 450 GeV, as expected from the logarithmic structure of Eq. (4.1). This effect is enhanced by the sign difference in the interference term, leading to a destructive or constructive interference, respectively. This is the dominant top mass effect in this channel, thus the one we want to use for a further signal–background analysis.

4.3 Signal–Background Analysis

We now know where top mass effects occur. We can use this information to perform a signal–background analysis similar to the analysis in the boosted Higgs regime. To gain sensitivity we need to suppress mainly the qq background. The gg continuums background is already part of the reference points $k_{(t,g)} = (1, 0)$ and $k_{(t,g)} = (0, 1)$.

We normally do not have any spin correlations between production and decay of the Higgs since the Higgs seems to favour the scalar hypothesis. However, in the background interference term $2\mathcal{R}e(\mathcal{M}_c\mathcal{M}_{g(t)})$ spin correlation are still present. This makes the Cabibbo–Maksymowicz–Dell'Aquila–Nelson angles [123–126] an interesting set of observables to suppress the background. With those five angles it is possible to capture the complete kinematics of the $H \to ZZ \to 4\ell$ process, including correlations with the incoming protons. The Nelson

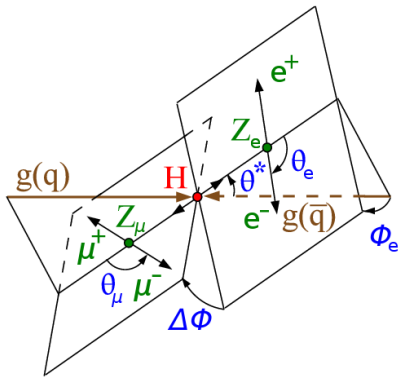

Figure 4.4: Representation of the Nelson angles defined in Eq. (4.13) for the $gg(q\bar{q}) \to H \to ZZ \to e^+e^-\mu^+\mu^-$ process.

angles are defined in case of two final state lepton pairs of different flavour as

$$\begin{aligned} \cos\theta_e &= \hat{p}_{e^-} \cdot \hat{p}_{Z_\mu}\Big|_{Z_e} & \cos\phi_e &= \left(\hat{p}_{\text{beam}} \times \hat{p}_{Z_\mu}\right) \cdot \left(\hat{p}_{Z_\mu} \times \hat{p}_{e^-}\right)\Big|_{Z_e} \\ \cos\theta_\mu &= \hat{p}_{\mu^-} \cdot \hat{p}_{Z_e}\Big|_{Z_\mu} & \cos\Delta\phi &= \left(\hat{p}_{e^-} \times \hat{p}_{e^+}\right) \cdot \left(\hat{p}_{\mu^-} \times \hat{p}_{\mu^-}\right)\Big|_{H} \\ \cos\theta^* &= \hat{p}_{Z_e} \cdot \hat{p}_{\text{beam}}\Big|_{H} \end{aligned} \tag{4.13}$$

where the Z and Higgs momenta are reconstructed with

$$p_{Z_\mu} = p_{\mu^+} + p_{\mu^-} \qquad p_{Z_e} = p_{e^+} + p_{e^-} \qquad p_H = p_{Z_\mu} + p_{Z_e}. \tag{4.14}$$

The vertical line $\Big|_x$ indicates that the 4–momenta are boosted into the rest frame of particle x.

The normalized Nelson angle distributions of the different relevant contributions are shown in Fig. 4.5, as well as a figurative representation in Fig. 4.4. Since we are interested in the highly off-shell region we applied the cut $m_{4\ell} > 600$ GeV beforehand. We see that $\cos\theta^*$ has a high potential in differentiating between the qq initiated background and those with a gg initial state. The polarization angles $\cos\phi_e$ and $\cos\phi_\mu$ on the other hand show a discrimination power between the SM and HEFT approximation hypothesis.

In principle the kinematics of an event can be completely reconstructed. This can be used to plug the information back into the matrix elements of the different possible origins of an event in order to get a probability value. With this a log–likelihood ratio can be constructed which can to some extend differentiate between signal and background. This is known as matrix–element likelihood approach. However, in our case we want to keep the analysis as simple as possible. We use therefore $|\cos\theta^*| < 0.7$ to suppress the qq initiated background and $\cos\phi_e$ as an additional descriminant to $m_{4\ell}$. With the 2–dimensional correlation between $\cos\phi_e$ and $m_{4\ell}$ we preform a shape analysis, analogue to what we did in the boosted Higgs regime.

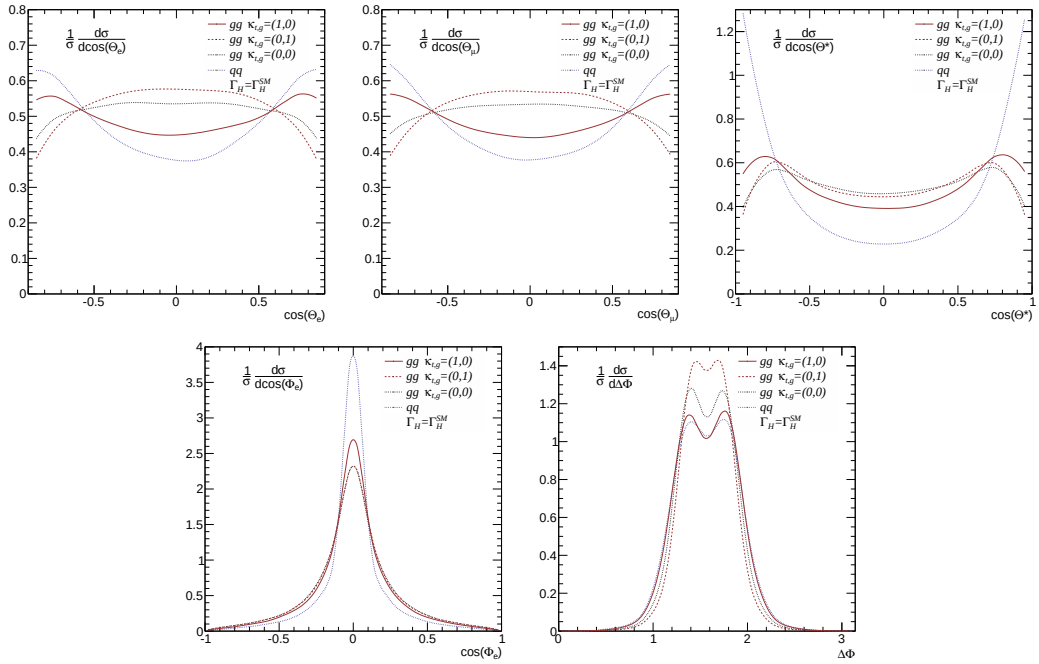

Figure 4.5: Normalized Nelson angles distributions for the $gg \to ZZ$ for the different signal hypothesis $\kappa_{(t,g)}$ and the dominant background $qq \to ZZ$ for $m_{4\ell} > 600$ GeV. We assume the LHC at $\sqrt{s} = 13$ TeV.

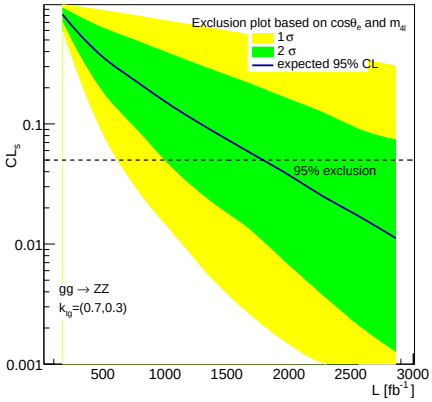

Figure 4.6: Confidence level for separating the BSM hypotheses $\kappa_{t,g} = (0.7, 0.3)$ from the Standard Model. We show results for $gg \to ZZ$ decays based on the 2D distribution $(\cos\theta_e, m_{4\ell})$.

We used the same setup, *i.e* MCLIMIT [110–112] within ROOT [76]. The Standard Model with corresponding backgrounds is defined to be the null hypothesis and we used the parameter set $k_{(t,g)} = (0.7, 0.3)$ as our BSM model. We present results for an idealized measurement by neglecting any systematic or theory uncertainties in Fig. 4.6. But even with this optimistic

assumption the off–shell measurement does not have the sensitivity when comparing it to the results of the boosted regime in Fig. 3.12 and Fig. 3.13. Constraining the Higgs–gluon coupling via other channels seems to be more promising.

4.4 Width Measurement

As mentioned it was recently proposed to use information from the off-shell regime as a direct measurement of the Higgs width [53–57]. The original idea behind this is as follows. The differential Higgs production cross section for a decay to a Z pair can be written as

$$\frac{d\sigma}{dm_{ZZ}} \propto g_{ggH}^2 g_{HZZ}^2 \frac{F(m_{ZZ})}{(m_{ZZ}^2 - m_H^2)^2 + m_H^2 \Gamma_H^2}. \tag{4.15}$$

g_{ggH} and g_{HZZ} are the usual coupling constants from the Higgs to gluons and Zs, respectively. The function F depends on the kinematics of the production and decay. The integrated cross section can then be written separately for the on–shell and off-shell region as

$$\begin{aligned} \sigma^{\text{on–shell}} &\propto \frac{g_{ggH}^2(m_H) g_{HZZ}^2(m_H)}{\Gamma_H} \qquad \text{and} \\ \sigma^{\text{off–shell}} &\propto g_{ggH}^2(m_{4\ell}) g_{HZZ}^2(m_{4\ell}). \end{aligned} \tag{4.16}$$

The on–shell rate is invariant under a scaling the coupling constants $g = g_{ggH}, g_{HZZ}$ and of the Higgs width,

$$\Gamma_H = \xi^4 \Gamma_H^{\text{SM}} \qquad \text{and} \qquad g = \xi g^{\text{SM}}, \tag{4.17}$$

which is known as ξ–degeneracy. The off–shell region on the other hand is dependent on such a scaling. It was proposed to use this feature as a direct measurement of the Higgs width.

This idea, however, is in general strongly model–dependent, as pointed out shortly after by [127]. Our parameterization provides a good example where this procedure does not work. We obtain

$$\begin{aligned} \sigma^{\text{on–shell}} &\propto \left(\kappa_t^2 + \kappa_g^2\right) \frac{g_{ggH}^2(m_H) g_{HZZ}^2(m_H)}{\Gamma_H} \qquad \text{and} \\ \sigma^{\text{off–shell}} &\propto \left(\kappa_t g_{ggH}(m_{4\ell}) + \kappa_g g_{ggH}(m_H)\right)^2 g_{HZZ}^2. \end{aligned} \tag{4.18}$$

Since $\kappa_t + \kappa_g = 1$ holds, the on–shell rate will not be affected by any change in the parameters κ_t and κ_g. The off-shell rate however, develops an non–trivial dependence on the parameters set. This is because the effective coupling g_{ggH} is only a constant number if all external particles are on their respective mass shell. The coupling therefore does not factorize in the κ_g and κ_t components.

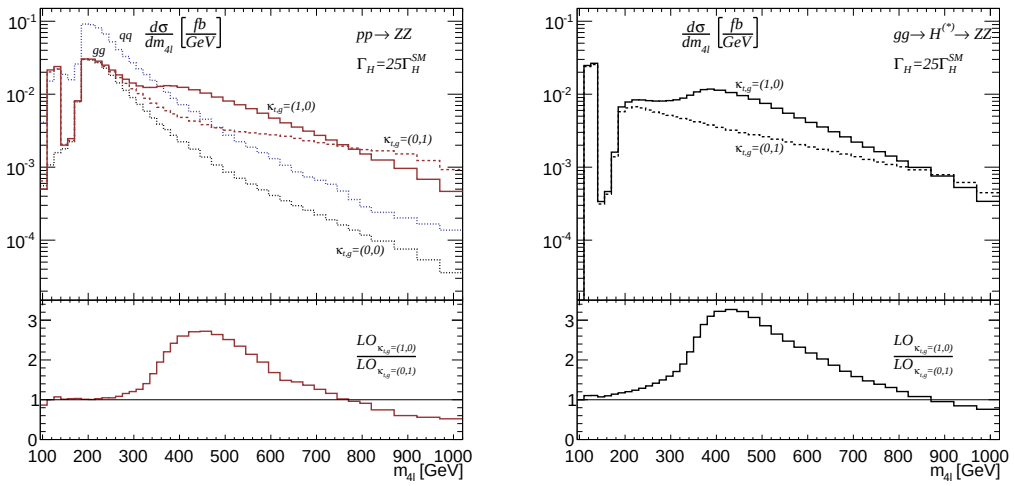

Figure 4.7: $m_{4\ell}$ distributions for the $gg \to ZZ$ (left) and $gg \to H \to ZZ$ (right) for the different signal hypothesis and the dominant background. We assume the LHC at $\sqrt{s} = 13$ TeV.

To illustrate this dependence we rescaled the Higgs width and couplings by

$$\xi^4 = 25 \qquad \to \qquad \Gamma_H = 25\Gamma_H^{\mathrm{SM}}. \tag{4.19}$$

We present the outcome in Fig. 4.7, which can be directly compared to the previous scenario with $\xi^4 = 1$ in Fig. 4.2. We see on the right panel that the on–shell peak has not changed its size as expected, but off–shell regime did. Moreover, when including the continuum background and its interference with the signal we observe in the left panel of Fig. 4.7 a completely different shape than what we got with $\xi^4 = 1$, see left panel of Fig. 4.2.

This shows that a measurement of the Higgs width is strongly entangled with the parameters κ_t and κ_g. When interpreting the current off–shell rate measurements as a measurement of the Higgs width we therefore need to assume the pure Standard Model parameter set $k_{(t,g)} = (1, 0)$. An additional contribution will significantly spoil those measurements.

5 Conclusion and Outlook

In this thesis we discussed top mass effects in the Higgs–gluon coupling in two different regimes, boosted and off-shell.

For a boosted Higgs we showed that top mass dependent logarithms lead to a splitting between a Standard Model scenario and a pure dimension–6 hypothesis in p_T spectra when the Higgs is produced in association with two jets. The effect of absorptive terms in the invariant masses are negligible. We showed that the logarithmic structure of the Hjj case is very similar to the Hj process. The dominant contribution seems to be a VBF–like topology with highly virtual gluons from initial state partons. An even higher jet–multiplicity is unlikely to have a numerically and fundamentally new effect. Despite the similarity between the origin of top mass effects, thus a numerically very similar difference between the SM and BSM scenario, the Hjj process has a higher rate in the sensitive region than the Hj process.

Using two basic analyses for the $\tau\tau$ and WW decay channel, we showed that the Hjj process does not only benefits from the second jet in rate, but also in background rejection. With a shape analysis we computed exclusion limits based in the different p_T spectra in order to compare the decay channels as well as the sensitivity of the observables. We obtained that the transverse momentum of the Higgs performs better than the p_T of the leading jet. Both decay channels lead to similar exclusion limits. We therefore conclude that the Hjj process is not just a correction to the Hj process, but has a high rate in the top mass sensitive region and offers very useful analysis handles.

Having showed the importance of the Hjj process we examined top mass effects in a fully merged analysis. With merged LO H+jets samples we found that the logarithmic top mass effects factorize in each jet bin and that it converges to a constant factor in the low–energy regime. We obtain the same result when adding NLO corrections to this sample. The NLO K–factor is p_T dependent and around 2. It does not factorize for the Standard Model hypothesis and the dimension–6 scenario in the boosted regime, thus the ratio between both hypotheses is slightly reduced. Nevertheless, we showed that not only NLO corrections but also top mass effects play a vital role in simulating p_T spectra.

Since the top mass effects in the NLO samples show only some numerical differences to the previous performed analysis, the next step is obviously to redo this analysis. Due to time constraints this is not done yet, but we are currently working on it. Ideally the analysis is

modified such that all jet bins are taken into account. This is straight forward for the first set of cuts, but the sensitivity 2–jet correlation observables are to be checked again. Ultimately the NLO sample can be compared with the previous results and the boosted section by computing exclusion limits. It is likely that the exclusion limit can be improved by using the p_T distribution splitted in a 1–jet and 2–jet subsample for a 2–dimensional correlation shape analysis.

In off-shell Higgs production in the $pp(\to H) \to ZZ \to 4\ell$ channel, which gets sizeable due to several threshold enhancements, develops a logarithmic dependence on the top mass in the differential invariant mass $m_{4\ell}$ distribution. We obtain a destructive interference for the Standard Model scenario, but a constructive interference for the pure dimension–6 scenario in the invariant mass distributions $m_{4\ell}$. The $m_{4\ell}$ distribution of the pure signal component shows a large threshold enhancement due to the top mass around 350 GeV, however, it is negligible in the total gg initial state including the continuum background and interference. The main top mass effect occurs due to $m_{4\ell}$ in the far off–shell regime. The signal benefits from the $gg \to H \to ZZ$ interference with the $gg \to ZZ$ continuum background and we obtain a splitting between both hypotheses around 450 GeV.

Using the Cabibbo–Maksymowicz–Dell'Aquila–Nelson angles to suppress the $qq \to ZZ$ background we found with a 2–dimensional shape analysis that the off–shell regime is not as sensitive to top mass effects than the boosted regime. This is mainly due to the small rates in the region of interest. We also provided an example for the model dependence of the recently proposed Higgs width measurement. We showed that with our parameterization the width measurement is strongly correlated to a measurement of the parameters κ_g and κ_t. Because they can not be disentangled the method used by the CMS collaboration needs to assume a pure Standard Model scenario without any new physics contributing to the Higgs–gluon coupling.

Acknowledgements

First, I want to thank Tilman Plehn for giving me the opportunity to write my master's thesis abroad at the IPPP in Durham, for support and guidance, as well as for this really interesting project.

Special thanks goes to Dorival Gonçalves. To keep it short, since it would fill pages otherwise: It was a pleasure to work with you and I definitely owe you some drinks next time I am in Durham!

Of course I also want to thank my other collaborators - Christoph Englert, Frank Krauss, Silvan Kuttimalai, Marek Schönherr und Michael Spannowsky - there were a lot of helpful discussions! Also I would like to thank Peter Richardson for his support in my first months in Durham, even though our work unfortunately does not found its way into this thesis.

Thank you also to everybody in OC118 - Dan, Darren, John, Mark, Ryan and Tom - I will miss this absolutely crazy working environment! Last but not least thank you to everybody I met in Durham and who made this year truly memorable!

A Appendix

Here we want to show, that the Higgs+1–jet matrix element $\mathcal{M}_{+++}$ quoted in Eq. (3.6) develops indeed powers of $\ln(p_T^2/m_t^2)$ in the high–p_T limit. Since the matrix element is rather lengthy the aim of this paragraph is not to simplify the formula as far as possible, but to get an insight into the structure and where the logarithms are coming from. We therefore perform the calculation in the high–p_T limit until the first logarithms appear. We start by quoting the analytical form of the amplitude [48]

$$\begin{aligned}\frac{\mathcal{M}_{+++}}{m_t^2\Delta} = &-64\left(\frac{1}{ut}+\frac{1}{tt_1}+\frac{1}{uu_1}\right)-\frac{64}{s}\left(\frac{2s+t}{u_1^2}B_1(u)+\frac{2s+u}{t_1^2}B_1(t)\right)\\ &-16\frac{s-4m_t^2}{stu}\left[s_1C_1(s)+(u-s)C_1(t)+(t-s)C_1(u)\right]-128m_t^2\left(\frac{1}{tt_1}C_1(t)+\frac{1}{uu_1}C_1(u)\right)\\ &+\frac{64m_t^2}{s}D(u,t)+8\frac{s-4m_t^2}{stu}\left[stD(s,t)+usD(u,s)-utD(u,t)\right]-\frac{32}{s^2}E(u,t). \quad \text{(A.1)}\end{aligned}$$

s,t and u are the usual Mandelstam variables and

$$s_1 = s-m_H^2, \qquad t_1 = t-m_H^2, \qquad u_1 = u-m_H^2 \qquad \text{and} \qquad \Delta = \sqrt{\frac{1}{8}stu}. \qquad \text{(A.2)}$$

In the limit of $m_t^2, m_H^2 \ll p_T^2, s, |t|, |u|$ of course $s_1 = s$, $t_1 = t$ and $u_1 = u$ holds, where

$$s+t+u = 0 \qquad \text{and} \qquad p_T^2 = \frac{tu}{s}. \qquad \text{(A.3)}$$

The functions B_1, C_1 and D are basic scalar integrals and E is an auxiliary function.

B_1 is given as a combination of the scalar two–point function B by

$$B_1(x) = B(x) - B(m_H^2). \qquad \text{(A.4)}$$

B itself can be written as

$$\begin{aligned}B(x) &= -\int_0^1 dw \ln\left(m_t^2 - i\epsilon - xw(1-w)\right)\\ &= -\left[\ln\left(m_t^2\right) - 2 + (2a(x)-1)\ln\left(\frac{a(x)}{a(x)-1}\right)\right]\\ &\approx -\left[\ln\left(m_t^2\right) - 2 + \ln\left(\frac{|x|}{m_t^2}\right) + i\pi\Theta(x)\right] \qquad \text{(A.5)}\end{aligned}$$

with the Heaviside function Θ and

$$a(x) = \frac{1}{2}\left(1 + \sqrt{1 - \frac{4\left(m_t^2 - i\epsilon\right)}{x}}\right). \tag{A.6}$$

The approximation in the last step of Eq. (A.5) holds only for $m_t^2 \ll |x|$ and therefore not for $B(m_H^2)$. B can develop an imaginary part since the physical region is $s \geq 0$ and $t, u \leq 0$, which may lead to complex logarithms.

The scalar three–point function C can be expressed as

$$\begin{aligned} C(x) &= \int_0^1 \frac{dw}{wx} \ln\left(1 - i\epsilon - \frac{x}{m_t^2} w(1-w)\right) \\ &= \frac{1}{2x} \ln^2\left(\frac{a(x)}{a(x)-1}\right) \\ &\approx \frac{1}{2x}\left[\ln^2\left(\frac{|x|}{m_t^2}\right) + 2\pi i \Theta(x) \ln\left(\frac{|x|}{m_t^2}\right) - \pi^2 \Theta(x)\right] \end{aligned} \tag{A.7}$$

where the approximation again holds only in the $m_t^2 \ll |x|$ limit. C_1 is then given by

$$x_1 C_1(x) = xC(x) - m_H^2 C(m_H^2). \tag{A.8}$$

For the scalar four–point function $D(x, y)$ we use z for the Mandelstam variable, which is not already part of the argument of D. The scalar integral is then given by

$$D(x,y) = \frac{1}{xy}\left[I_{xyz}(x) + I_{yxz}(y) - I_{xyz}(m_H^2)\right] \tag{A.9}$$

where

$$\begin{aligned} I_{xyz}(v) =& \int_0^1 \frac{dw}{w(1-w) + m_t^2 z/xy} \ln\left(1 - i\epsilon - \frac{v}{m_t^2} w(1-w)\right) \\ =& \frac{2}{\sqrt{1 + 4m_t^2 z/xy}}\left[\mathrm{Li}_2\left(\frac{x_-}{x_- - a(v)}\right) - \mathrm{Li}_2\left(\frac{x_+}{x_+ - a(v)}\right) + \mathrm{Li}_2\left(\frac{x_-}{a(v) - x_+}\right)\right. \\ & \left. - \mathrm{Li}_2\left(\frac{x_+}{a(v) - x_-}\right) + \ln\left(\frac{-x_-}{x_+}\right) \ln\left(1 - i\epsilon - \frac{v}{m_t^2} x_- x_+\right)\right] \end{aligned} \tag{A.10}$$

with

$$x_\pm = \frac{1}{2}\left(1 \pm \sqrt{1 + \frac{4m_t^2 z}{xy}}\right). \tag{A.11}$$

Li_2 is the dilogarithm or Spence's function. With the series expansion of the single and

dilogarithms in the high–p_T limit up to $\mathcal{O}\left(\frac{m_t^2}{x}\right)$,

$$\begin{aligned}
&\mathrm{Li}_2\left(\frac{x_-}{x_- - a(x)}\right) = 0, \qquad \mathrm{Li}_2\left(\frac{x_+}{x_+ - a(x)}\right) = \mathrm{Li}_2\left(-\frac{z}{x}\right), \qquad \mathrm{Li}_2\left(\frac{x_-}{a(x) - x_+}\right) = \frac{\pi^2}{6}, \\
&\mathrm{Li}_2\left(\frac{x_+}{x_+ - a(x)}\right) = -\frac{\pi^2}{6} - \frac{1}{2}\left[\ln\left(\frac{|y|}{m_t^2}\right) + i\pi\left(\Theta(x) - \Theta(xy)\right)\right]^2 \quad \text{and} \\
&\ln\left(\frac{-x_-}{x_+}\right)\ln\left(1 - i\epsilon - \frac{x}{m_t^2}x_- x_+\right) = \left[\ln\left(\frac{|x|}{|y|} + i\pi\Theta(xy)\right)\right]\left[\ln\left(\frac{|z|\,m_t^2}{|x|\,|y|}\right) + i\pi\left(2 - \Theta(zy) - \Theta(x)\right)\right],
\end{aligned} \tag{A.12}$$

we conclude that the four–point functions can be written as

$$\begin{aligned}
D(s,t) &= \frac{1}{st}\left[2\mathrm{Li}_2\left(-\frac{u}{s}\right) + 2\mathrm{Li}_2\left(-\frac{u}{t}\right) + \ln^2\left(\frac{|t|}{m_t^2}\right) + \ln^2\left(\frac{s}{m_t^2}\right) - 5\pi^2 + 2i\pi\ln\left(\frac{|t|\,u^2 m_t^2}{s^4}\right) - I(m_H)\right] \\
D(u,t) &= \frac{1}{ut}\left[2\mathrm{Li}_2\left(-\frac{s}{u}\right) + 2\mathrm{Li}_2\left(-\frac{s}{t}\right) + \ln^2\left(\frac{|t|}{m_t^2}\right) + \ln^2\left(\frac{|u|}{m_t^2}\right) - 10\pi^2 + 2i\pi\ln\left(\frac{s m_t^6}{t^2 u^2}\right) - I(m_H)\right]
\end{aligned} \tag{A.13}$$

with

$$I(m_H) = -2\mathrm{Li}_2\left(\frac{1}{1 - a(m_H)}\right) - 2\mathrm{Li}_2\left(\frac{1}{a(m_H)}\right). \tag{A.14}$$

The function $D(s,u)$ is obtained by exchanging u and t in $D(s,t)$.

The auxiliary function E is given by

$$E(u,t) = uC(u) + tC(t) + u_1 C(u_1) + t_1 C(t_1) - utD(u,t). \tag{A.15}$$

When we now reshuffle the terms in the matrix element of Eq. (A.1) slightly and apply some high–p_T approximations,

$$\begin{aligned}
\frac{\mathcal{M}_{+++}}{m_t^2\Delta} = &-64\frac{s^2 - ut}{u^2 t^2} - \frac{64}{s}\left(\frac{2s+t}{u^2}B_1(u) + \frac{2s+u}{t^2}B_1(t)\right) - 16\frac{s}{tu}C(s) \\
&-16\left(\frac{t-s}{tu} + \frac{4u}{s^2}\right)C(u) + 16\frac{m_H^2}{tu}\left(1 + \frac{u-s}{t} + \frac{t-s}{u} + \frac{4tu}{s^2}\right)C(m_H^2) \\
&-16\left(\frac{u-s}{tu} + \frac{4t}{s^2}\right)C(t) - 8\left(1 - 4\frac{ut}{s^2}\right)D(u,t) + 8\frac{s}{u}D(s,t) + 8\frac{s}{t}D(s,u),
\end{aligned} \tag{A.16}$$

we see that we have now all information we need. Inserting the scalar integrals we get

$$\begin{aligned}
\frac{\mathcal{M}_{+++}}{m_t^2\Delta} &= -64\frac{s^2+3ut}{u^2t^2} + \frac{128}{ut}\left(\ln\left(m_t^2\right) + B(m_H)\right) - \frac{64}{s}\left(\frac{2s+t}{u^2}\ln\left(\frac{|u|}{m_t^2}\right) + \frac{2s+u}{t^2}\ln\left(\frac{|t|}{m_t^2}\right)\right) \\
&\quad -\frac{8}{tu}\left(\ln^2\left(\frac{s}{m_t^2}\right) + 2i\pi\ln\left(\frac{s}{m_t^2}\right) - \pi^2\right) + 16\frac{m_H^2}{tu}\left(1 + \frac{u-s}{t} + \frac{t-s}{u} + \frac{4tu}{s^2}\right)C(m_H^2) \\
&\quad -8\left(\frac{t-s}{tu^2} + \frac{4}{s^2}\right)\ln^2\left(\frac{|u|}{m_t^2}\right) - 8\left(\frac{u-s}{t^2u} + \frac{4}{s^2}\right)\ln^2\left(\frac{|t|}{m_t^2}\right) \\
&\quad -8\left(\frac{1}{ut} - 4\frac{1}{s^2}\right)\left[\ln^2\left(\frac{|t|}{m_t^2}\right) + \ln^2\left(\frac{|u|}{m_t^2}\right) - 10\pi^2 + 2i\pi\ln\left(\frac{sm_t^6}{t^2u^2}\right) - I(m_H)\right] \\
&\quad +8\frac{1}{ut}\left[\ln^2\left(\frac{|t|}{m_t^2}\right) + \ln^2\left(\frac{s}{m_t^2}\right) - 5\pi^2 + 2i\pi\ln\left(\frac{|t|\,u^2m_t^2}{s^4}\right) - I(m_H)\right] \\
&\quad +8\frac{1}{ut}\left[\ln^2\left(\frac{|u|}{m_t^2}\right) + \ln^2\left(\frac{s}{m_t^2}\right) - 5\pi^2 + 2i\pi\ln\left(\frac{|u|\,t^2m_t^2}{s^4}\right) - I(m_H)\right] \\
&\quad -16\left(\frac{1}{ut} - 4\frac{1}{s^2}\right)\left[\mathrm{Li}_2\left(-\frac{s}{u}\right) + \mathrm{Li}_2\left(-\frac{s}{t}\right)\right] \\
&\quad +16\frac{1}{ut}\left[\mathrm{Li}_2\left(-\frac{u}{s}\right) + \mathrm{Li}_2\left(-\frac{u}{t}\right) + \mathrm{Li}_2\left(-\frac{t}{s}\right) + \mathrm{Li}_2\left(-\frac{t}{u}\right)\right] \\
&= -64\frac{s^2+3ut}{u^2t^2} + \frac{128}{ut}\left(\ln\left(m_t^2\right) + B(m_H)\right) - \frac{64}{s}\left(\frac{2s+t}{u^2}\ln\left(\frac{|u|}{m_t^2}\right) + \frac{2s+u}{t^2}\ln\left(\frac{|t|}{m_t^2}\right)\right) \\
&\quad +\frac{8\pi^2}{tu} + 16\frac{m_H^2}{tu}\left(1 + \frac{u-s}{t} + \frac{t-s}{u} + \frac{4tu}{s^2}\right)C(m_H^2) \\
&\quad -\frac{8}{tu}\left[\frac{t-s}{u}\ln^2\left(\frac{|u|}{m_t^2}\right) + \frac{u-s}{t}\ln^2\left(\frac{|t|}{m_t^2}\right) - \ln^2\left(\frac{s}{m_t^2}\right)\right] \\
&\quad -\frac{32}{s^2}\left[+10\pi^2 + 2i\pi\ln\left(\frac{p_T^2}{s}\right) + I(m_H)\right] + 8\frac{1}{ut}\left[10i\pi\ln\left(\frac{p_T^2}{s}\right) - I(m_H)\right] \\
&\quad -16\left(\frac{1}{ut} - 4\frac{1}{s^2}\right)\left[\mathrm{Li}_2\left(-\frac{s}{u}\right) + \mathrm{Li}_2\left(-\frac{s}{t}\right)\right] \\
&\quad +16\frac{1}{ut}\left[\mathrm{Li}_2\left(-\frac{u}{s}\right) + \mathrm{Li}_2\left(-\frac{u}{t}\right) + \mathrm{Li}_2\left(-\frac{t}{s}\right) + \mathrm{Li}_2\left(-\frac{t}{u}\right)\right] \qquad \text{(A.17)}
\end{aligned}$$

Using the identity

$$\mathrm{Li}_2\left(-\frac{x}{y}\right) + \mathrm{Li}_2\left(-\frac{x}{z}\right) = -\frac{1}{2}\ln^2\left(\frac{|y|}{|z|}\right) + \Theta(yz)\left(\frac{\pi^2}{2} + i\pi\ln\left(\frac{|y|\,|z|}{x^2}\right)\right) \qquad \text{(A.18)}$$

we can simplify the matrix element to

$$\begin{aligned}\frac{\mathcal{M}_{+++}}{m_t^2\Delta} =& -64\frac{s^2+3ut}{u^2t^2}+\frac{128}{ut}\left(\ln\left(m_t^2\right)+B(m_H)\right)-\frac{64}{s}\left(\frac{2s+t}{u^2}\ln\left(\frac{|u|}{m_t^2}\right)+\frac{2s+u}{t^2}\ln\left(\frac{|t|}{m_t^2}\right)\right)\\ &+16\frac{m_H^2}{tu}\left(1+\frac{u-s}{t}+\frac{t-s}{u}+\frac{4tu}{s^2}\right)C(m_H^2)\\ &+\frac{16}{tu}\left[\frac{s}{u}\ln^2\left(\frac{|u|}{m_t^2}\right)+\frac{s}{t}\ln^2\left(\frac{|t|}{m_t^2}\right)-\ln^2\left(\frac{s}{m_t^2}\right)-\ln^2\left(\frac{p_T^2}{m_t^2}\right)\right]\\ &-\frac{32}{s^2}\left[+9\pi^2+I(m_H)\right]+8\frac{1}{ut}\left[8i\pi\ln\left(\frac{p_T^2}{s}\right)-I(m_H)\right]\end{aligned} \tag{A.19}$$

This formula shrinks together even further when we use the relation $s\sim 4p_T^2$ in the high–p_T limit [48]. From Eq. (A.3) then follows $t=u=-2p_T^2$ and we get

$$\begin{aligned}\mathcal{M}_{+++} =&\sqrt{8}\frac{m_t^2}{p_T}\left[+24-16\pi-9\pi^2-16\ln\left(\frac{m_H^2}{m_t^2}\right)-24\ln(2)-6\ln^2(2)-16i\pi\ln(2)\right.\\ &\left.+16m_H^2C(m_H^2)-2I(m_H)+24\left[1+\ln(2)\right]\ln\left(\frac{p_T^2}{m_t^2}\right)-20\ln^2\left(\frac{p_T^2}{m_t^2}\right)\right].\end{aligned} \tag{A.20}$$

We therefore see that the matrix element scales indeed with powers of $\ln\left(p_T^2/m_t^2\right)$.

B Bibliography

[1] G. Aad *et al.* [ATLAS Collaboration], Phys. Lett. B **716**, 1 (2012),

[2] S. Chatrchyan *et al.* [CMS Collaboration], Phys. Lett. B **716**, 30 (2012).

[3] P. W. Higgs, *Broken symmetries, massless particles and gauge fields,* Phys. Lett. **12**, 132 (1964);

[4] P. W. Higgs, *BROKEN SYMMETRIES AND THE MASSES OF GAUGE BOSONS,* Phys. Rev. Lett. **13**, 508 (1964);

[5] P. W. Higgs, *Spontaneous Symmetry Breakdown Without Massless Bosons,* and Phys. Rev. **145**, 1156 (1964);

[6] F. Englert and R. Brout, *BROKEN SYMMETRY AND THE MASS OF GAUGE VECTOR MESONS,* Phys. Rev. Lett. **13**, 321 (1964);

[7] G.S. Guralnik, C.R. Hagen and T.W. Kibble, *Global Conservation Laws And Massless Particles,* Phys. Rev. Lett. **13**, 585 (1964).

[8] CMS Collaboration, *Constraints on the Higgs boson width from off-shell production and decay to $ZZ \to \ell\ell\ell\ell$ and $\ell\ell\nu\nu$,* CMS-PAS-HIG-14-002 (2013).

[9] ATLAS Collaboration, *Evidence for the spin–0 nature of the Higgs boson using ATLAS data,* Phys. Lett. B **726**, 120 (2013)

[10] M. Shaposhnikov and C. Wetterich, *Asymptotic safety of gravity and the Higgs boson mass,* Phys. Lett. B **683**, 196 (2010);

[11] M. Holthausen, K. S. Lim and M. Lindner, *Planck scale Boundary Conditions and the Higgs Mass,* JHEP **1202**, 037 (2012);

[12] A. Hebecker, A. K. Knochel and T. Weigand, *The Higgs mass from a String-Theoretic Perspective,* Nucl. Phys. B **874**, 1 (2013);

[13] D. Buttazzo *et al*, *Investigating the near-criticality of the Higgs boson,* JHEP **1312**, 089 (2013).

[14] A. Belyaev and L. Reina, *$pp \to t\bar{t}H$,$H \to \tau^+\tau^-$: Toward a model independent determination of the Higgs boson couplings at the LHC,* JHEP **0208**, 041 (2002);

[15] E. Gross and L. Zivkovic, *$t\bar{t}H \to t\bar{t}\tau\tau$: Toward the Measurement of the top-Yukawa Coupling,* Eur. Phys. J. **59**, 731 (2009);

[16] T. Plehn, G. P. Salam and M. Spannowsky, *Fat Jets for a Light Higgs,* Phys. Rev. Lett. **104** (2010) 111801;

[17] C. Boddy, S. Farrington and C. Hays, *Higgs boson coupling sensitivity at the LHC using $H \to \tau\tau$ decays,* Phys. Rev. D **86**, 073009 (2012);

[18] P. Artoisenet, P. de Aquino, F. Maltoni and O. Mattelaer, *Unravelling $t\bar{t}h$ via the Matrix Element Method,* Phys. Rev. Lett. **111** (2013) 9, 091802;

[19] P. Agrawal, S. Bandyopadhyay and S. P. Das, *Dilepton Signatures of the Higgs Boson with Tau-jet Tagging,* arXiv:1308.6511 [hep-ph].

[20] M. R. Buckley, T. Plehn, T. Schell and M. Takeuchi, *Buckets of Higgs and Tops,* JHEP **1402**, 130 (2014).

[21] M. Farina, C. Grojean, F. Maltoni, E. Salvioni and A. Thamm, *Lifting degeneracies in Higgs couplings using single top production in association with a Higgs boson,* JHEP **1305**, 022 (2013);

[22] S. Biswas, E. Gabrielli, F. Margaroli and B. Mele, *Direct constraints on the top-Higgs coupling from the 8 TeV LHC data,* JHEP **07**, 073 (2013);

[23] J. Ellis, D. S. Hwang, K. Sakurai and M. Takeuchi, *Disentangling Higgs-Top Couplings in Associated Production,* JHEP **1404** (2014) 004;

[24] C. Englert and E. Re, *Bounding the top Yukawa with Higgs-associated single-top production,* Phys. Rev. D **89**, 073020 (2014).

[25] W. J. Stirling and D. J. Summers, *Production of an intermediate mass Higgs boson in association with a single top quark at LHC and SSC,* Phys. Lett. B **283**, 411 (1992).

[26] F. Maltoni, D. L. Rainwater and S. Willenbrock, *Measuring the top quark Yukawa coupling at hadron colliders via $t\bar{t}H, H \to W^+W^-$,* Phys. Rev. D **66** (2002) 034022.

[27] M. Klute, R. Lafaye, T. Plehn, M. Rauch and D. Zerwas, *Measuring Higgs Couplings from LHC Data,* Phys. Rev. Lett. **109**, 101801 (2012);

[28] D. Lopez-Val, T. Plehn and M. Rauch, *Measuring Extended Higgs Sectors as a Consistent Free Couplings Model,* JHEP **1310**, 134 (2013).

[29] The ATLAS collaboration, ATLAS-CONF-2012-170.

[30] The CMS collaboration, CMS-PAS-HIG-12-045.

[31] A. Azatov, R. Contino and J. Galloway, *Model-Independent Bounds on a Light Higgs,* JHEP **1204**, 127 (2012);

[32] P. P. Giardino, K. Kannike, M. Raidal and A. Strumia, *Is the resonance at 125 GeV the Higgs boson?,* Phys. Lett. B **718**, 469 (2012);

[33] J. Ellis and T. You, *Global Analysis of the Higgs Candidate with Mass 125 GeV,* JHEP **1209**, 123 (2012);

[34] J. R. Espinosa, C. Grojean, M. M}uhlleitner and M. Trott, JHEP **1205**, 097 (2012), JHEP **1209**, 126 (2012) 126, and *First Glimpses at Higgs' face,* JHEP **1212**, 045 (2012);

[35] A. Djouadi and G. Moreau, *The couplings of the Higgs boson and its CP properties from fits of the signal strengths and their ratios at the 7+8 TeV LHC,* arXiv:1303.6591 [hep-ph];

[36] J. Ellis and T. You, *Updated Global Analysis of Higgs Couplings,* JHEP **1306**, 103 (2013).

[37] A. Azatov and J. Galloway, *Electroweak Symmetry Breaking and the Higgs Boson: Confronting Theories at Colliders,* Int. J. Mod. Phys. A **28** (2013) 1330004;

[38] I. Brivio *et al.*, *Disentangling a dynamical Higgs,* JHEP **1403** (2014) 024;

[39] R. Contino, M. Ghezzi, C. Grojean, M. Mühlleitner and M. Spira, *Effective Lagrangian for a light Higgs-like scalar,* JHEP **1307** (2013) 035;

[40] J. Elias-Miro, J. R. Espinosa, E. Masso and A. Pomarol, *Higgs windows to new physics through d=6 operators: constraints and one-loop anomalous dimensions,* JHEP **1311** (2013) 066;

[41] C. Englert, A. Freitas, M. Mühlleitner, T. Plehn, M. Rauch, M. Spira and K. Walz, *Precision Measurements of Higgs Couplings: Implications for New Physics Scales,* arXiv:1403.7191 [hep-ph];

[42] J. Ellis, V. Sanz and T. You, *Complete Higgs Sector Constraints on Dimension-6 Operators,* arXiv:1404.3667 [hep-ph].

[43] J. R. Ellis, M. K. Gaillard and D. V. Nanopoulos, *A Phenomenological Profile of the Higgs Boson,* Nucl. Phys. B **106**, 292 (1976);

[44] M. A. Shifman, A. I. Vainshtein, M. B. Voloshin and V. I. Zakharov, *Low-Energy Theorems for Higgs Boson Couplings to Photons,* Sov. J. Nucl. Phys. **30**, 711 (1979) [Yad. Fiz. **30**, 1368 (1979)];

[45] B. A. Kniehl and M. Spira, *Low-energy theorems in Higgs physics,* Z. Phys. C **69**, 77 (1995).

[46] T. Plehn, *Lectures on LHC Physics,* Lect. Notes Phys. **844**, 1 (2012).

[47] R. K. Ellis, I. Hinchliffe, M. Soldate and J. J. van der Bij, *Higgs Decay to tau+ tau-: A Possible Signature of Intermediate Mass Higgs Bosons at the SSC,* Nucl. Phys. B **297**, 221 (1988).

[48] U. Baur and E. W. N. Glover, *Higgs Boson Production at Large Transverse Momentum in Hadronic Collisions,* Nucl. Phys. B **339**, 38 (1990).

[49] M. Schlaffer, M. Spannowsky, M. Takeuchi, A. Weiler and C. Wymant, *Boosted Higgs Shapes,* arXiv:1405.4295 [hep-ph].

[50] C. Englert, M. McCullough and M. Spannowsky, *Gluon-initiated associated production boosts Higgs physics,* Phys. Rev. D **89**, 013013 (2014).

[51] A. Banfi, A. Martin and V. Sanz, *Probing top-partners in Higgs + jets,* arXiv:1308.4771 [hep-ph].

[52] A. Azatov and A. Paul, *Probing Higgs couplings with high p_T Higgs production,* JHEP **1401**, 014 (2014).

[53] N. Kauer and G. Passarino, *Inadequacy of zero-width approximation for a light Higgs boson signal,* JHEP **1208**, 116 (2012);

[54] F. Caola and K. Melnikov, *Constraining the Higgs boson width with ZZ production at the LHC,* Phys. Rev. D **88**, 054024 (2013);

[55] J. M. Campbell, R. K. Ellis and C. Williams, *Bounding the Higgs width at the LHC using full analytic results for $gg- > e^-e^+\mu^-\mu^+$,* JHEP **1404**, 060 (2014).

[56] V. Khachatryan *et al.* [CMS Collaboration], *Constraints on the Higgs boson width from off-shell production and decay to Z-boson pairs,* Phys. Lett. B **736**, 64 (2014);

[57] ATLAS collaboration, *Determination of the off-shell Higgs boson signal strength in the high-mass ZZ final state with the ATLAS detector,* ATLAS-CONF-2014-042.

[58] CMS Collaboration, *Properties of the Higgs-like boson in the decay $H \to ZZ \to 4\ell$ in pp collisions at $\sqrt{s} = 7$ and 8 TeV,* CMS-PAS-HIG-13-002 (2013).

[59] E. W. N. Glover and J. J. van der Bij, *Z Boson Pair Production Via Gluon Fusion,* Nucl. Phys. B **321**, 561 (1989).

[60] A. Azatov, C. Grojean, A. Paul and E. Salvioni, *Taming the off-shell Higgs boson,* arXiv:1406.6338 [hep-ph].

[61] D. Graudenz, M. Spira and P. M. Zerwas, *QCD corrections to Higgs boson production at proton proton colliders,* Phys. Rev. Lett. **70**, 1372 (1993);

[62] M. Spira, A. Djouadi, D. Graudenz and P. M. Zerwas, *Higgs boson production at the LHC,* Nucl. Phys. B **453**, 17 (1995);

[63] M. Krämer, E. Laenen and M. Spira, *Soft gluon radiation in Higgs boson production at the LHC,* Nucl. Phys. B **511**, 523 (1998);

[64] S. Marzani, R. D. Ball, V. Del Duca, S. Forte and A. Vicini, *Higgs production via gluon-gluon fusion with finite top mass beyond next-to-leading order,* Nucl. Phys. B **800**, 127 (2008),

[65] A. Pak, M. Rogal and M. Steinhauser, *Finite top quark mass effects in NNLO Higgs boson production at LHC,* JHEP **1002**, 025 (2010).

[66] R. V. Harlander, T. Neumann, K. J. Ozeren and M. Wiesemann, *Top-mass effects in differential Higgs production through gluon fusion at order α_s^4,* JHEP **1208**, 139 (2012);

[67] M. Spira, *QCD effects in Higgs physics,* Fortsch. Phys. **46**, 203 (1998).

[68] LHC Higgs Cross Section Working Group, *Handbook of LHC Higgs Cross Sections: 3. Higgs Properties,* arXiv:1307.1347 [hep-ex].

[69] J. C. Collins, D. E. Soper and G. F. Sterman, *Factorization of Hard Processes in. QCD,* Adv. Ser. Direct. High Energy Phys. 5 (1988) 1?91, [hep-ph/0409313]

[70] J. M. Campbell, R. K. Ellis, R. Frederix, P. Nason, C. Oleari and C. Williams, *NLO Higgs Boson Production Plus One and Two Jets Using the POWHEG BOX, MadGraph4 and MCFM,* JHEP **1207** (2012) 092.

[71] J. M. Campbell, R. K. Ellis and C. Williams, MCFM web page `http://mcfm.fnal.gov`

[72] F. Campanario, M. Kubocz and D. Zeppenfeld, *Gluon-fusion contributions to Phi + 2 Jet production,* Phys. Rev. D **84**, 095025 (2011);

[73] J. Baglio, J. Bellm, F. Campanario, B. Feigl, J. Frank, T. Figy, M. Kerner and L. D. Ninh *et al.*, *Release Note - VBFNLO 2.7.0,* arXiv:1404.3940 [hep-ph].

[74] K. Arnold, M. Bahr, G. Bozzi, F. Campanario, C. Englert, T. Figy, N. Greiner and C. Hackstein *et al.*, *VBFNLO: A Parton level Monte Carlo for processes with electroweak bosons,* Comput. Phys. Commun. **180** (2009) 1661.

[75] J. Pumplin, D. R. Stump, J. Huston, H. L. Lai, P. M. Nadolsky and W. K. Tung, *New generation of parton distributions with uncertainties from global QCD analysis,* JHEP **0207**, 012 (2002) [hep-ph/0201195].

[76] R. Brun and F. Rademakers, *ROOT – An Object Oriented Data Analysis Framework,* Nucl. Inst. & Meth. in Phys. Res. A **389**, (1997) 81-86, Proceedings AIHENP'96 Workshop, Lausanne, Sept. 1996, See also: http://root.cern.ch/.

[77] T. Gleisberg, S. .Hoeche, F. Krauss, M. Schönherr, S. Schumann, F. Siegert and J. Winter, *Event generation with SHERPA 1.1,* JHEP **0902**, 007 (2009)

[78] T. Gleisberg and S. Hoeche, *Comix, a new matrix element generator,* JHEP **0812**, 039 (2008);

[79] S. Hoeche, F. Krauss, M. Schönherr and F. Siegert, *A critical appraisal of NLO+PS matching methods,* JHEP **1209**, 049 (2012);

[80] S. Hoche, F. Krauss, M. Schönherr and F. Siegert, *NLO matrix elements and truncated showers,* JHEP **1108**, 123 (2011);

[81] S. Hoeche, F. Krauss, M. Schönherr and F. Siegert, *QCD matrix elements + parton showers: The NLO case,* JHEP **1304**, 027 (2013);

[82] S. Hoeche, F. Krauss and M. Schönherr, *Uncertainties in MEPS@NLO calculations of h+jets,* arXiv:1401.7971 [hep-ph].

[83] A. Denner and S. Dittmaier, *Scalar one-loop 4-point integrals,* Nucl. Phys. B **844**, 199 (2011) [arXiv:1005.2076 [hep-ph]].

[84] J. M. Campbell, R. K. Ellis and G. Zanderighi, *Next-to-Leading order Higgs + 2 jet production via gluon fusion,* JHEP **0610** (2006) 028;

[85] J. M. Campbell, R. K. Ellis and C. Williams, *Hadronic production of a Higgs boson and two jets at next-to-leading order,* Phys. Rev. D **81** (2010) 074023;

[86] H. van Deurzen, N. Greiner, G. Luisoni, P. Mastrolia, E. Mirabella, G. Ossola, T. Peraro and J. F. von Soden-Fraunhofen *et al.*, *NLO QCD corrections to the production of Higgs plus two jets at the LHC,* Phys. Lett. B **721**, 74 (2013).

[87] C. Grojean, E. Salvioni, M. Schlaffer and A. Weiler, *Very boosted Higgs in gluon fusion,* arXiv:1312.3317 [hep-ph].

[88] E. Boos and T. Plehn, *Higgs boson production induced by bottom quarks,* Phys. Rev. D **69**, 094005 (2004).

[89] V. Del Duca, W. Kilgore, C. Oleari, C. Schmidt and D. Zeppenfeld, *Higgs + 2 jets via gluon fusion,* Phys. Rev. Lett. **87**, 122001 (2001);

[90] V. Del Duca, W. Kilgore, C. Oleari, C. Schmidt and D. Zeppenfeld, *Gluon fusion contributions to H + 2 jet production,* Nucl. Phys. B **616**, 367 (2001).

[91] T. Sjostrand, S. Mrenna and P. Z. Skands, *PYTHIA 6.4 Physics and Manual,* JHEP **0605**, 026 (2006).

[92] J. Alwall*et al. A standard format for Les Houches Event Files,* Comput. Phys. Commun. **176**, 300-304 (2007).

[93] S. Frixione, P. Nason and C. Oleari, *Matching NLO QCD computations with Parton Shower simulations: the POWHEG method,* JHEP **0711**, 070 (2007);

[94] T. Melia, P. Nason, R. Rontsch and G. Zanderighi, *W+W-, WZ and ZZ production in the POWHEG BOX,* JHEP **1111**, 078 (2011);

[95] P. Nason, *A New method for combining NLO QCD with shower Monte Carlo algorithms* JHEP **0411**, 040 (2004);

[96] H.–L. Lai, M. Guzzi, J. Huston,Z. Li, P. M. Nadolsky, J. Pumplin, C.–P. Yuan, *New parton distributions for collider physics,* Phys. Rev. D **82**, 074024 (2010);

[97] S. Frixione and B. R. Webber, *Matching NLO QCD computations and parton shower simulations,* JHEP **0206**, 029 (2002) [hep-ph/0204244].

[98] C. F. Berger, Z. Bern, L. J. Dixon, F. Febres Cordero, D. Forde, H. Ita, D. A. Kosower and D. Maitre, *An Automated Implementation of On-Shell Methods for One-Loop Amplitudes,* Phys. Rev. D **78**, 036003 (2008);

[99] M. Cacciari, G. P. Salam and G. Soyez, *The Anti-k(t) jet clustering algorithm,* JHEP **0804**, 063 (2008);

[100] M. Cacciari, G. P. Salam and G. Soyez, *FastJet User Manual,* Eur. Phys. J. C **72**, 1896 (2012).

[101] ATLAS Collaboration, *Calibration of the performance of b–taggin for c and light–flavour jets in the 2012 ATLAS data,* ATLAS–CONF–2014–046 (2014).

[102] T. Plehn, D. L. Rainwater and D. Zeppenfeld, *Determining the structure of Higgs couplings at the LHC,* Phys. Rev. Lett. **88**, 051801 (2002);

[103] C. Ruwiedel, N. Wermes and M. Schumacher, *Prospects for the measurement of the structure of the coupling of a Higgs boson to weak gauge bosons in weak boson fusion with the ATLAS detector,* Eur. Phys. J. C **51**, 385 (2007);

[104] G. Klamke and D. Zeppenfeld, *Higgs plus two jet production via gluon fusion as a signal at the CERN LHC,* JHEP **0704** (2007) 052;

[105] K. Hagiwara, Q. Li and K. Mawatari, *Jet angular correlation in vector-boson fusion processes at hadron colliders,* JHEP **0907**, 101 (2009);

[106] C. Englert, D. Gonçalves-Netto, K. Mawatari and T. Plehn, *Higgs Quantum Numbers in Weak Boson Fusion,* JHEP **1301**, 148 (2013);

[107] C. Englert, D. Gonçaclves, G. Nail and M. Spannowsky, *The shape of spins,* Phys. Rev. D **88**, 013016 (2013);

[108] K. Hagiwara and S. Mukhopadhyay, *Azimuthal correlation among jets produced in association with a bottom or top quark pair at the LHC,* JHEP **1305**, 019 (2013);

[109] M. R. Buckley, T. Plehn and M. J. Ramsey-Musolf, *Stop on Top,* arXiv:1403.2726 [hep-ph].

[110] Tom Junk, *Sensitivity, Exclusion and discovery with Small Signals, Large Backgrounds, and Large Systematic Uncertainties,* CDF/DOC/STATISTICS/PUBLIC/8128 (2007)

[111] Tom Junk, *Building a More General* χ^2, CDF/DOC/STATISTICS/PUBLIC/7904 (2007)

[112] Tom Junk, *Bayesian limit software: multi–channel with correlated backgrounds and efficiencies,* CDF/MEMO/STATISTICS/PUBLIC/7587 (2005)

[113] S. Catani and F. Krauss and R. Kuhn and B. R. Webber, *QCD matrix elements + parton showers,* JHEP **11** (2001) 063

[114] L. Lönnblad, *Correcting the color dipole cascade model with fixed order matrix elements,* JHEP **05** (2002) 046

[115] J. Alwall, M. Herquet, F. Maltoni, O. Mattelaer and T. Stelzer, *MadGraph 5 : Going Beyond,* JHEP **1106**, 128 (2011) [arXiv:1106.0522 [hep-ph]].

[116] S. Hoeche, F. Krauss, M. Schönherr and F. Siegert, *QCD matrix elements + parton showers: The NLO case,* JHEP **1304**, 027 (2013) [arXiv:1207.5030 [hep-ph]].

[117] J. M. Campbell, R. K. Ellis and C. Williams, *Bounding the Higgs width at the LHC: complementary results from* $H \to WW$, Phys. Rev. D **89**, 053011 (2014).

[118] J. S. Gainer, J. Lykken, K. T. Matchev, S. Mrenna and M. Park, *Beyond Geolocating: Constraining Higher Dimensional Operators in* $H \to 4\ell$ *with Off-Shell Production and More,* arXiv:1403.4951 [hep-ph].

[119] G. Cacciapaglia, A. Deandrea, G. D. La Rochelle and J. B. Flament, *Higgs couplings: disentangling New Physics with off-shell measurements,* arXiv:1406.1757 [hep-ph].

[120] I. Anderson, S. Bolognesi, F. Caola, Y. Gao, A. V. Gritsan, C. B. Martin, K. Melnikov and M. Schulze *et al.*, *Constraining anomalous HVV interactions at proton and lepton colliders,* Phys. Rev. D **89**, 035007 (2014) [arXiv:1309.4819 [hep-ph]].

[121] G. Passarino, *Higgs precision physics: the next step,* PoS RADCOR **2013**, 049 (2013).

[122] R. E. Cutkosky, *Singularities and Discontinuities of Feynman Amplitudes,* J. Math. Phys. 1, **429** (1960).

[123] N. Cabibbo and A. Maksymowicz, "Angular Correlations in Ke-4 Decays and Determination of Low-Energy pi-pi Phase Shifts," Phys. Rev. **137**, B438 (1965) [Erratum-ibid. **168**, 1926 (1968)];

[124] J. R. Dell'Aquila and C. A. Nelson, "P OR CP DETERMINATION BY SEQUENTIAL DECAYS: V1 V2 MODES WITH DECAYS INTO anti-lepton (A) lepton (B) AND/OR anti-q (A) q (B)," Phys. Rev. D **33**, 80 (1986);

[125] J. R. Dell'Aquila and C. A. Nelson, "DISTINGUISHING A SPIN 0 TECHNIPION AND AN ELEMENTARY HIGGS BOSON: V1 V2 MODES WITH DECAYS INTO anti-lepton (A) lepton (B) AND/OR anti-q (A) q (B)," Phys. Rev. D **33**, 93 (1986);

[126] C. A. Nelson, "Correlation Between Decay Planes In Higgs Boson Decays Into W Pair (into Z Pair)," Phys. Rev. D **37**, 1220 (1988).

[127] C. Englert and M. Spannowsky, *Limitations and Opportunities of Off-Shell Coupling Measurements*, arXiv:1405.0285 [hep-ph].

Erklärung:

Ich versichere, dass ich diese Arbeit selbstständig verfasst habe und keine anderen als die angegebenen Quellen und Hilfsmittel benutzt habe.

Heidelberg, den (Datum) .....